Title: Non-redundant cardiolipin synthases support membrane integrity and stress resilience in *Bacteroides fragilis*

Authors: Matthew K. Schnizlein[1], Bong Jin Hong[1,2], Jennifer N.T. Nguyen[3], Katarina Jones[4,5], Alyssa I. Rodriguez[3], Aretha Fiebig[1,6], Shawn R. Campagna[4,5], Marcy J. Balunas[3,7], Thomas V. O'Halloran[1,2,8], Sean Crosson[1,6,*]

*corresponding author: crosson4@msu.edu

Affiliations

[1]Department of Microbiology, Genetics & Immunology, Michigan State University, East Lansing, MI, USA

[2]Elemental Health Institute, Michigan State University, East Lansing, MI, USA

[3]Department of Medicinal Chemistry, University of Michigan, Ann Arbor, MI, USA

[4]Biological and Small Molecule Mass Spectrometry Core, University of Tennessee-Knoxville, TN, USA

[5]Department of Chemistry, University of Tennessee-Knoxville, TN, USA

[6]BioMolecular Science Gateway, Michigan State University, East Lansing, MI, USA

[7]Department of Microbiology and Immunology, University of Michigan, Ann Arbor, MI, USA

[8]Department of Chemistry, Michigan State University, East Lansing, MI, USA

Abstract: *Bacteroides fragilis* is an anaerobic resident of the human gut known to tolerate the toxic effects of host-produced and microbially-modified bile acids. Two putative cardiolipin synthases, ClsA and ClsB, have been linked to bile acid tolerance in *B. fragilis*, yet their specific physiological roles remain undefined. Although ClsA and ClsB are conserved across *Bacteroides*

species, they are phylogenetically distinct from the well-characterized cardiolipin synthases of Gammaproteobacteria and Firmicutes. Here, we show that these enzymes have distinct cardiolipin synthase activities and make non-redundant contributions to *B. fragilis* fitness under gut-relevant stress conditions, including osmotic stress, disruption of membrane potential, and exposure to the bile acid deoxycholate. While deoxycholate disrupted K^+/Na^+ homeostasis in *B. fragilis*, deletion of *clsA* or *clsB* did not significantly alter intracellular ion levels, suggesting that loss of cardiolipin synthase function does not directly impact ion balance under standard cultivation conditions. High resolution mass spectrometry-based lipidomic analyses showed that cardiolipin comprises less than 1% of *B. fragilis* membranes and that ClsA and ClsB produce distinct cardiolipin products with unique acyl chain lengths and levels of unsaturation. Deletion of either *cls* gene led to Cls-specific remodeling of *B. fragilis* envelope lipid content, which was also associated with shifts in non-lipid metabolites indicative of stress-induced metabolic changes. These results demonstrate distinct roles for ClsA and ClsB in shaping *B. fragilis* membrane composition, metabolism, and stress responses and offer new insight into how bile acids impact the physiology of a common member of the gut microbiota.

Importance: Inflammatory bowel diseases are a growing global health concern, motivating efforts to understand how inflammation-associated microbes, such as *Bacteroides fragilis*, adapt to and persist in stress conditions characteristic of the inflamed intestinal environment. Through genetic analyses of targeted mutants, we show that the cardiolipin synthases ClsA and ClsB make distinct, non-redundant contributions to *B. fragilis* fitness under bile acid stress and other gut-relevant conditions. Through a combination of omics approaches, we further show that these enzymes produce chemically distinct cardiolipin species, and that their loss leads to specific alterations in membrane lipid composition and cellular metabolome profiles. Our study shows how cardiolipin synthases shape membranes and metabolic systems that impact *B. fragilis* resilience in conditions encountered in the gut environment.

53

54 **INTRODUCTION**

55 To successfully occupy gut niches and maintain homeostasis, bacteria must preserve
56 membrane integrity to resist phage attack, host immune pressures, and membrane-disrupting
57 molecules such as bile acids (1-7). The functional properties of membranes are shaped by the
58 diverse lipids classes of which they are made, each characterized by an array of structural species
59 (8-10). For example, bacteria can alter their membrane fluidity and/or permeability by modulating
60 the length of phospholipid acyl tails in response to extracellular conditions (8, 11). Bacteria also
61 adjust the abundance of different phospholipid types or modify lipid headgroups through reactions
62 such as aminoacylation (12-16).

63 In addition to protecting against external threats, membranes also help support cellular
64 metabolism by maintaining a potential energy source in the form of ion gradients, such as
65 hydrogen (protons, H^+), sodium (Na^+), and potassium (K^+) (17). One of the best-known functions
66 of proton gradients is to power rotary ATPase complexes (i.e., F_oF_1) associated with aerobic and
67 anaerobic respiration (18-22). Prokaryotes as well as eukaryotes maintain Na^+ and K^+ at
68 intracellular concentrations that are lower and higher, respectively, relative to their environment,
69 which drives the transport of metals or other molecules across the membrane (23, 24).

70 Cardiolipins, which make up 1–5% of the bacterial membrane, play an integral role in
71 maintaining ion gradients (25-30). This class of membrane lipid comprises two covalently bonded
72 phospholipids, such as phosphatidylglycerol (PG) or in some cases phosphatidylethanolamine
73 (PE) (31). While cardiolipins increase proton permeability across model liposome membranes
74 (28, 32), they also contribute to membrane stabilization by enhancing hydrogen bonding, reducing
75 water permeability and sustaining membrane potential during stress-induced membrane
76 depolarization (32, 33). In addition, several protein complexes require cardiolipin for proper
77 function, including some two-component systems, protein translocation machinery, and
78 respiratory complexes (34-39).

79 *Escherichia coli* has three well-studied genes responsible for cardiolipin biosynthesis:
80 *clsA*, *clsB* and *clsC* (31, 40). Each gene makes distinct contributions to *E. coli* physiology
81 depending on growth phase, with *clsA* being the primary *cls* used during logarithmic (log)-phase
82 growth and all three used during stationary phase (26, 31). While ClsA and ClsB act on PG as the
83 sole substrate, ClsC synthesizes cardiolipin from PE as well as PG (31, 41-43). The Cls enzymes
84 encoded by these genes are thought to synthesize three structural families of cardiolipin, which
85 have four (cardiolipin), three (monolysocardiolipin) and two acyl tails (dilysocardiolipin),
86 respectively (for chemical structures, see Fig. 6A) (44). However, mechanistic insight into bacterial
87 cardiolipin biosynthesis and function largely comes from studies in *E. coli* and other
88 Enterobacteriaceae. Expanding this research across diverse bacterial lineages is essential for
89 uncovering the broader physiological roles of this important lipid class.

90 The gut microbe *Bacteroides fragilis* is a gram-negative facultative anaerobe that must
91 maintain membrane integrity for gut fitness (45-47). While *B. fragilis* strains, particularly those that
92 carry the fragilysin toxin, are linked to colorectal cancer and other diseases (48), it constitutes
93 about 1–5% of the microbiota in otherwise healthy humans (49, 50). We recently identified two
94 cardiolipin synthases as critical for the survival of the non-toxigenic *B. fragilis* strain P207 in the
95 presence of physiologically relevant levels of deoxycholate, a secondary bile acid (51). *B. fragilis*
96 P207 was isolated from the ileoanal pouch of a patient with ulcerative colitis (UC) and is
97 representative of *B. fragilis* populations that can dominate prior to the onset of pouchitis (52), a
98 condition characterized by UC-like inflammation of the ileoanal pouch following colectomy (53).
99 In this study, we build on our previous findings by investigating the roles of the two *B. fragilis*
100 cardiolipin synthases across a broader range of membrane stress conditions. Since cardiolipin
101 synthases are largely uncharacterized in the Bacteroidota, our work provides foundational
102 knowledge about this important class of enzymes in a dominant group of gut microbes (54). Using
103 a combination of approaches, we demonstrate that the two *cls* genes in *B. fragilis* P207, *clsA* and
104 *clsB*, are evolutionarily and functionally distinct from *cls* homologs in *E. coli* and other well-studied

105 bacterial phyla. These genes encode non-redundant enzymes that contribute structurally unique
106 cardiolipin species to the membrane, conferring distinct physiological advantages under stress.
107 We further show that *clsA* and *clsB* differ in their expression profiles and that mutants lacking
108 each gene produce distinct cardiolipin species as well as distinct metabolomic profiles, supporting
109 complementary roles in maintaining membrane homeostasis and adapting to diverse
110 environmental conditions.

111

112 **RESULTS**

113 **B. fragilis *P207 ClsA and ClsB are cardiolipin synthases***

114 The two *B. fragilis* P207 genes, ptos_000612 (*clsA*) and ptos_003252 (*clsB*), encode
115 proteins with predicted cardiolipin synthase domains (TIGR04265, PFAM13091, cd09112),
116 though *clsA* and *clsB* have low nucleotide (52.4%) and amino acid sequence (29.6%) identity to
117 each other (Fig. 1A). The low primary structure identity (≤30%) of ClsA and ClsB to *E. coli* Cls
118 proteins limited our ability to predict their specific enzymatic activities based on sequence alone
119 (Fig. 1A). Furthermore, *E. coli* ClsC did not align well with ClsA or ClsB from either *B. fragilis* or
120 *E. coli* (Fig. 1A, B). We therefore excluded ClsC from further comparisons.

121 ClsA and ClsB from *B. fragilis* and *E. coli* exhibit high amino acid conservation in two
122 regions around their predicted active sites but share limited identity across the remainder of the
123 protein (Fig. 1B, C). The Cls proteins from both species harbor two phospholipase-D active site
124 motifs H-X-K-X(4)-D (26, 42), indicative of phospholipase-D activity (Fig. 1D). Indeed, deleting
125 either *clsA* (Δ*clsA*) or *clsB* (Δ*clsB*) in *B. fragilis* resulted in a partial loss of cellular cardiolipin
126 accumulation relative to the wild-type (WT) strain; deleting both genes (Δ*clsA* Δ*clsB*) completely
127 abolished cardiolipin accumulation (Fig. 1E). We conclude that *clsA* and *clsB* in *B. fragilis* P207
128 encode *bona fide* cardiolipin synthases. A more comprehensive analysis of how deletion of *clsA*

129 and *clsB* affects the membrane lipid composition of the *B. fragilis* envelope is presented in
130 sections below.
131
132 ***The cardiolipin synthases* of Bacteroides *sp. occupy a distinct phylogenetic cluster among***
133 ***dominant gut bacterial phyla***
134 To evaluate the relatedness between *Bacteroides* Cls proteins and those encoded by other
135 gut microbes, we performed pairwise alignments of Cls sequences from dominant bacterial phyla
136 present in the human gut. These sequences clustered according to their evolutionary heritage,
137 except for the Bacillota, which had two clusters (Fig. 1F). Based on this result, we conclude that
138 each cardiolipin synthase originated from a proto-lineage, rather than having been horizontally
139 transferred.
140 We next evaluated Cls protein sequences within the *Bacteroides* genus. We aligned 301
141 *Bacteroides* protein sequences containing the TIGR04265 domain (i.e. cardiolipin synthases).
142 Most genomes encoded two cardiolipin synthases that partitioned into distinct clusters (Fig. S1).
143 Notably, the *B. thetaiotaomicron* genome encodes a third Cls that is distinct from the other two
144 *Bacteroides* Cls clusters (Fig S1) indicating an evolutionarily distant introduction. We designate
145 cluster 1 homologs as ClsA based on our observation that both *B. fragilis* and *E. coli* ClsA proteins
146 are predicted to have two N-terminal transmembrane helices, suggesting a similar mode of post-
147 translational processing (55, 56). We named the cluster 2 homologues ClsB, as they represent
148 proteins from the second and only other annotated *cls* gene in most *Bacteroides*. We left the third
149 *cls* gene, which we identified only in *B. thetaiotaomicron*, unnamed and did not further
150 characterize it.
151 Within the *Bacteroides* genus, the chromosomal gene neighborhoods around *clsA* (Fig.
152 S2A) and *clsB* (Fig. S2B) are highly conserved; this conservation is lost outside the *Bacteroides*.
153 Thus, the genomic context of *clsA* and *clsB* provides some indication of the identity of each *cls*
154 gene, specifically within the *Bacteroides* lineage. This evidence also supports the hypothesis that

155 taxa inherited each *cls* gene in two distinct regions of the chromosome. Considering this
156 phylogeny, our analysis of the *B. fragilis cls* genes presented below offer insight into the function
157 of the two broadly distributed cardiolipin synthases across the genus *Bacteroides*.
158
159 **clsA *and* clsB *deletion mutants have growth defects under membrane stress***
160 To explore the functions of the two cardiolipin synthases in *B. fragilis* P207, we generated
161 mutant strains harboring in-frame deletions of *clsA* (Δ*clsA*) and *clsB* (Δ*clsB*), and a strain lacking
162 both *cls* genes (Δ*clsA* Δ*clsB*). We also generated corresponding genetic complementation strains
163 bearing *clsA* or *clsB* integrated at a neutral heterologous site in the chromosome. We assessed
164 the growth characteristics of these *B. fragilis* strains under stress conditions that perturb various
165 aspects of membrane biology (Fig. 2). The treatments in this study included: 1) the detergents
166 deoxycholate and sodium dodecyl sulfate (SDS); 2) low pH; 3) the salts NaCl and KCl; and 4) the
167 ionophores monensin A (for Na^+) and nigericin (for K^+ and H^+) to disrupt transmembrane ion
168 gradients. Treatment concentrations were chosen based on their effect on WT strain growth.
169 In the absence of treatment, all strains grew equally well (Figs. 2A, S3A, B). Treatment
170 with the detergents deoxycholate (at 0.01% [w/v]; Fig. 2A, S3) or SDS (at 0.002% [w/v]) (Fig. 2B)
171 limited the growth of the *cls* mutant strains to a greater extent than WT. Deoxycholate affected
172 maximum OD_{600} in the Δ*clsA* Δ*clsB* att::*clsA* strain, and both max OD_{600} and growth rate the Δ*clsA*
173 Δ*clsB* strain. SDS treatment mainly affected lag time, decreasing the max OD_{600} values in the first
174 20 h of growth. Doubling time defects appeared as little or no growth, rather than slower growth
175 (Fig. 2B). Under both detergent conditions, the deletion of *clsB* had a larger effect on fitness than
176 deletion of *clsA* (Figs. 2A, B, S3) and deletion of both genes (Δ*clsA* Δ*clsB*) had an additive effect.
177 300 mM K^+ or Na^+ (Fig. 2C, D) also lowered the growth rate and maximum OD_{600} of the mutant
178 strains relative to WT (Fig. S3). Both Δ*clsA* and Δ*clsB* strains exhibited similar phenotypes, with
179 the Δ*clsA* Δ*clsB* strain showing more pronounced effects. Lowering the medium pH from 6.9 to

180 pH 5.5 (i.e., higher [H^+]) had a detrimental effect on all *B. fragilis* strains, with no clear *cls*-
181 dependent growth defects (Fig. 2E).

182 The ionophores nigericin and monensin A dissipate ion gradients by mediating the
183 exchange of ions across the inner membrane (57, 58). Specifically, nigericin is a potassium-
184 selective ionophore and a H^+-K^+ antiporter, erasing both gradients by acidifying the cytoplasm and
185 moving K^+ out of the cell (57). Monensin A is a sodium-selective ionophore with a 16-fold
186 preference for Na^+ over K^+, but can also affect H^+ gradients (57-59). Under either nigericin or
187 monensin A treatment, *clsB* deletion decreased strain fitness relative to the WT (Fig. 2F, G).
188 However, strains harboring *clsB* but lacking *clsA* (Δ*clsA* and Δ*clsA* Δ*clsB* att::*clsB*) exhibited a
189 higher maximum OD_{600} relative to the WT (Fig. S3).

190 We conclude that deleting *clsB* results in greater fitness defects than loss of *clsA* under
191 membrane perturbations. Furthermore, a functional ClsA limits growth under nigericin and
192 monensin A treatment, as we observed increased culture density in the Δ*clsA* strains. These
193 growth phenotypes provide evidence that ClsA and ClsB have distinct roles in *B. fragilis*
194 membrane physiology.

195

196 ***Loss of cardiolipin changes cell shape***

197 Given that in many bacteria, cardiolipin influences cell division, morphology, and
198 membrane fluidity (60-67), we asked whether loss of Cls function in *B. fragilis* would affect cell
199 shape. Deletion of either *cls* gene did not markedly affect overall rod-like cell shape or cellular
200 length distribution (Fig. S4A, B). However, cells lacking *clsA* (i.e., Δ*clsA* and Δ*clsA* Δ*clsB* strains;
201 Figs. 3A, B and S4C) were narrower. While cells lacking *clsB* were not significantly narrower than
202 WT, this cell population did have a broader cell width distribution compared to WT, suggesting a
203 role for ClsB in cell size regulation (F-test, WT to Δ*clsB* $p = 0.019$, WT to Δ*clsA* Δ*clsB att:clsA* $p <$
204 0.001, WT variances compared to Δ*clsA* and Δ*clsA* Δ*clsB* were not significantly different; Figs. 3A

205 and S4C). Both phenotypes could be genetically complemented. These results demonstrate that
206 ClsA and ClsB influence cell width in *B. fragilis* (Fig. 3A, B).
207
208 **B. fragilis *cardiolipin synthase genes have distinct expression profiles***
209 Considering the unique phenotypes of the Δ*clsA* and Δ*clsB* mutant strains, we
210 hypothesized that these genes have distinct expression patterns. To test this idea, we quantified
211 *clsA* and *clsB* transcripts levels across growth phases and stress conditions. *clsB* transcript levels
212 were four-fold higher during logarithmic (log) phase growth than in stationary phase, while *clsA*
213 expression was two-fold higher in stationary phase (Fig. 4A). During logarithmic growth, deletion
214 of either *cls* gene did not affect the transcript levels of the other (Fig. 4B). However, in stationary
215 phase, the deletion of *clsA* led to an 8-fold increase in *clsB* transcripts. No change in *clsA*
216 transcripts were observed upon *clsB* deletion (Fig. 4B). We conclude that the two cardiolipin
217 synthase genes of *B. fragilis* have distinct, growth-phase dependent expression profiles and that
218 *clsB* transcript upregulation in the Δ*clsA* strain may compensate for loss of ClsA activity.
219 To test if membrane stress influences the expression of the *cls* genes, we subjected cells
220 to acute stress for 20 minutes and harvested RNA. While SDS treatment did not affect *cls*
221 transcript levels, we observed a two-fold increase in *clsA* expression and a small decrease in *clsB*
222 transcripts after 0.01% deoxycholate and 300 mM K^+ treatments (Fig. 4C) (51). Acidic pH did not
223 alter *cls* transcript levels, but basic pH did decrease transcript levels of both genes (Fig. 4C).
224 Finally, we detected differences under ionophore treatment, although the biological significance
225 of these smaller changes is unclear (Fig. 4C).
226
227 ***Loss of cardiolipin synthase genes does not have a major impact on homeostasis of major***
228 ***cellular elements***
229 As cardiolipins play an important role in maintaining membrane barrier integrity (25-27,
230 68, 69), we used inductively coupled plasma mass spectrometry (ICP-MS) to quantitatively define

231 amounts of certain elements in *B. fragilis* cells and measure the effect of ClsA and/or ClsB or
232 stress treatment on those elements. While cell washing is routinely used to prepare samples for
233 metal analysis, it can disrupt intracellular levels of elements (Fig. S5A). Therefore, we used a
234 wash-free ICP-MS assay to minimize perturbation during sample preparation, adapted here for
235 bacterial cultures (70). Using this approach, we found that *B. fragilis* P207 cells grown in
236 supplemented brain heart infusion (BHIS) medium contained 550 mM phosphorus (P), 430 mM
237 potassium (K), 98 mM sulfur and 63 mM sodium (Na) (Fig. S5C, medium elemental concentrations
238 shown in S5B).

239 To compare strains, we normalized intracellular element levels to phosphorus content, an
240 accepted practice in this type of analysis (71). This revealed no significant differences across the
241 *ΔclsA*, *ΔclsB*, or double-deletion strains in the relative levels of elements detected (Fig. 5A, B,
242 and S5C). Notably, given the lack of strain-dependent defects in CFU viability, we observed shifts
243 in relative phosphorus content per CFU across *cls* mutants that was consistent with differences
244 in the OD_{600}/CFU ratios (Fig. S5E-G). Furthermore, sulfur levels scaled proportionally with
245 phosphorus across samples (Fig. S5D and S5G). While P and S abundance can vary across
246 physiological states of the cell, they are tightly regulated (72, 73). Together, the elemental
247 composition and OD_{600} data suggest that *cls* deletion can alter the ability of *cls* deletion strains to
248 consistently form colonies.

249 Like most organisms, *B. fragilis* maintains a higher concentration of intracellular K^+ (+400
250 ΔmM) and lower concentration of intracellular Na^+ (-67 ΔmM) than the surrounding environment
251 (Fig. 5C, D). Exposure to deoxycholate, a microbially-modified bile acid, led to decreased
252 intracellular K^+ and increased Na^+ contents, providing evidence that this treatment indeed disrupts
253 transmembrane ion gradients in *B. fragilis* (Figs. 5C, D & S5I-J). The observed increase in
254 intracellular P per CFU (Fig. S5K) suggests that some of these changes could result from the
255 presence of non-viable cells (Fig. S5L), as these cells would retain the S and P mass associated
256 with large molecules like proteins and nucleotides, while smaller, more permeable elements would

257 be lost across damaged membranes (74, 75). Treatment with the sodium selective ionophore,
258 monensin A, did not affect K^+ levels but caused a 32 mM increase in intracellular Na^+ (Fig. 5C,
259 D). By contrast, treatment with the potassium selective ionophore, nigericin, caused no detectable
260 effect on either K^+ or Na^+ content, suggesting that nigericin may require more than 20 min to act
261 on *B. fragilis*, or that the cells quickly adapt to the imposed ionic disturbance (Fig. 5C, D).
262

263 ***Membrane lipid composition of WT* B. fragilis *P207***

264 Through tandem mass spectrometric-based lipidomics (MS/MS), we characterized lipid
265 species present in *B. fragilis* P207 membranes using both negative and positive electrospray
266 ionization modes. To get an overall picture of WT cell membranes, we calculated the relative peak
267 area abundance for lipids detected in negative ionization mode. This analysis revealed that WT
268 cell membranes were predominantly composed of phospholipids (47% of total peak areas) and
269 ceramides (42%). The remaining abundance consisted of saccharolipids, diacylglycerols and *N*-
270 acyl lipids (Figs. 6A & S6A). The major phospholipids were species of PE (37% of total peak
271 areas), PS (7.2%) and PG (1.5%) (Fig. 6A, B, Table S4). Cardiolipin species accounted for
272 approximately 0.33% of membrane lipids detected (Fig. 6B, C). Dominant ceramides were
273 ceramide phosphoethanolamine (31.7% of total peak area) and ceramide beta-hydroxy fatty acid-
274 dihydrosphingosine (8.6%). These results are consistent with previous studies on *Bacteroides*
275 membrane lipid contents (76-78).

276 Since cardiolipin synthases use phospholipids as substrates, we investigated the types of
277 PA, PE, PS and PG species. For PA, PS and PE, the dominant lipid types were fully saturated
278 (30:0), comprising 85.8%, 60.7% and 57.1% of their respective classes (Fig. S6B). The most
279 prevalent PG species was 32:0 (54.5%, Fig. S6B). *B. fragilis* membranes also contained
280 lysophospholipids at lower levels than their two-acyl tailed versions (Fig. 6A), the most abundant
281 species of which were fully saturated at C_{15} chains for lysophosphatidylethanolamine (LPE;
282 76.9%) and lysophosphatidylserine (LPS; 54.9%), and unsaturated at 18:3 for lysophosphatidic

283 acid (LPA; 70.5%) (Fig. S6C). Ether-linked lipids and cardiolipin lipid pools showed much greater
284 diversity in their constituent acyl chains (Fig. S6D–F).
285
286 **ClsA *and* ClsB *mutants have distinct cardiolipins profiles***
287 We compared the membrane lipid profiles of the *B. fragilis* P207 WT strain and the derived
288 Δ*clsA*, Δ*clsB*, and Δ*clsA* Δ*clsB* mutant strains (Fig. 1E). While the overall abundance of the
289 dominant lipid classes did not vary significantly among the WT and *cls* mutant strains (Fig. 6B),
290 abundances of cardiolipin and monolysocardiolipin were lower in the *cls* deletion mutants (CL and
291 MLCL; Fig. 6C). Total cardiolipin levels were lower in the Δ*clsA*, Δ*clsB*, and Δ*clsA* Δ*clsB* strains
292 compared to WT, with the double knockout strain having no measurable cardiolipin (Fig. 6C). We
293 detect lower MLCL levels only in strains lacking *clsB*, indicating that ClsB is primarily responsible
294 for their biosynthesis (Fig. 6C). Notably, the deletion of both *clsA* and *clsB* led to no change in the
295 detected dilysocardiolipin (DLCL), indicating that in contrast to *E. coli* where Cls proteins
296 synthesize these lipids, a different enzymatic pathway is responsible for biosynthesis of DLCLs in
297 *B. fragilis* (Figs. 6C and S6H) (31, 41).
298 Principal component analysis (PCA) of membrane lipid peak areas revealed that each
299 mutant strain clustered separately, indicating that ClsA and ClsB independently shape membrane
300 lipid composition, while the double knockout reflected the combined loss of both functions (Fig.
301 6D). K-means clustering of lipid changes in *cls* deletion mutants relative to WT identified four
302 distinct lipid subpopulations (Fig. 6E). Clusters 1 and 2 were composed almost entirely of
303 cardiolipin, monolysocardiolipin and hexosylceramides (i.e., cluster 1 = AHexCer, cluster 2 =
304 AHexCer, Hex2Cer, HexCer_HDS), and were absent in the Δ*clsA* Δ*clsB* double deletion strain.
305 On average, the peak area of lipids in cluster 3 was significantly lower in strains lacking ClsA,
306 while cluster 4 lipids were significantly higher in strains lacking ClsB (Fig. 7A). Lipids from cluster
307 1 were largely missing is strains without *clsB*, and lipids from cluster 2 were largely missing in
308 strains without *clsA*. We therefore refer to these as *clsB*- and *clsA*-associated lipid clusters,

309 respectively. From these results, we conclude that ClsA and ClsB catalyze the production of
310 distinct lipid species in *B. fragilis*, consistent with the unique phenotypes observed in their
311 respective deletion mutants (Fig. 2).
312
313 ***ClsA and ClsB differentially influence cardiolipin saturation and membrane composition***
314 To better understand the roles of ClsA and ClsB in cardiolipin biosynthesis, we analyzed
315 the acyl chain length and degree of unsaturation in CL and MLCL species from lipid clusters 1
316 and 2. The cardiolipins associated with ClsA and with ClsB exhibited a different distribution of
317 chain lengths, including a subset of longer species that were only detected when ClsB was
318 present (Figs. 7B and S7A). The major differences between ClsA- and ClsB-associated lipids
319 were in acyl chain unsaturation: ClsA-associated cardiolipins were enriched in species with 3 and
320 11 double bonds, whereas ClsB-associated cardiolipins were enriched with 1, 2, and 14 double
321 bonds (Fig. 7C & S7B). These unique lipid profiles provide evidence that ClsA and ClsB have
322 distinct substrate preferences.
323 To determine whether *cls* deletions alter the membrane lipidome globally, we performed
324 PCA on the lipid profiles of each sample excluding cardiolipins. This analysis showed that each
325 strain still clustered separately with an additive phenotype, suggesting broad ranging, *cls*-specific
326 changes (Fig. S7D). Upon loss of cardiolipin biosynthesis in *B. fragilis*, we observe altered
327 membrane lipid composition, including shortening the acyl chain length of
328 phosphatidylethanolamine (PE), phosphatidylglycerol (PG) and phosphatidylserine (PS) species
329 (Figs. 7D and S7D). This shift was coupled with increases in lipid acyl chains with a high number
330 of total unsaturations (Figs. 7E and S7E). The combined effect of shorter acyl chains and
331 increased unsaturation is predicted to alter membrane fluidity and permeability, potentially
332 compensating for cardiolipin loss. Additional remodeling occurred in non-phospholipid lipid
333 classes, with lipid families such as fatty acids (FAHFA) and hexosylceramides (HexCer-HDS)
334 more affected by *clsA* deletion, while *N*-acyl lipids (NAOrn, NAE, NAGlySer), phosphoceramides

335 (CerP), other hexosylceramides (AHexCer, Hex3Cer), and ether-linked glycolipids (EtherMGDG)
336 were more affected by *clsB* deletion (Fig. 7F–H). These patterns were confirmed by elastic net
337 regression, which distinguished the double mutant from WT based reductions in Cluster 1 (CL
338 75:3, AHexCer [O-22:6]51:9:2O) and Cluster 3 (PE O-38:0:2O) lipid species, as well as increases
339 in two Cluster 4 lipids (NAGlySer 29:0:1O, PC O-24:4:1O). Together, these results provide
340 evidence that ClsA and ClsB have distinct biosynthetic activities that contribute to cardiolipin
341 diversity, and that the loss of either enzyme perturbs the membrane lipidome in unique ways.
342 These broader shifts in membrane composition upon *cls* gene deletion likely underlie the distinct
343 phenotypes observed in each mutant strain.
344
345 ***ClsA and ClsB loss lead to distinct changes in non-lipid metabolites***
346 Since we observed distinct shifts in non-cardiolipin lipids, we hypothesized that these
347 shifts might extend to other *B. fragilis* metabolites under non-stressed conditions. Using LC-
348 tandem mass spectrometry (LC-MS/MS), we found that each strain had unique metabolite
349 profiles, with Δ*clsB* being the most distinct (Figs. 8A-C). Using publicly available databases, 56%
350 of all features were annotated, with 83% of those matches from small molecule databases.
351 Approximately 27% of the metabolomic features were not shared between all the strains, with
352 ~14% of the features only depleted in Δ*clsA*, Δ*clsB*, or Δ*clsA* Δ*clsB* (Fig. 8B). Notably, we observed
353 that the effect of *clsA* and *clsB* deletion is not additive, with *clsB* deletion showing the most
354 profound alterations on the metabolomic profiles by hierarchical clustering (Fig. 8C).
355 To determine metabolites that are associated with *cls* deletions, we performed pathway
356 enrichment analysis comparing feature abundances between the WT and double knockout strain.
357 As with the lipidomics analysis above, we identified fatty amides as the most differentially enriched
358 pathway, followed by the fatty esters and sphingolipids (Fig. S8). Several non-lipid classes were
359 also identified, including alkaloids, amino acids, amino sugars, benzoic acid esters, and
360 pyrimidines as the most differentially enriched pathways with high enrichment factors and

361 significant p-values (Fig. 8D). Analysis of amino acids and related compounds identified lipid-
362 conjugated homoserine lactones (HSLs) and fatty amides to be substantially changed in the
363 mutant strains (Figs 8E–F). The lipid-conjugated HSLs, which are small signaling molecules
364 crucial in quorum sensing (79), were mainly associated with *clsB* deletion. In these mutants, levels
365 of long-chain HSLs (e.g., *N*-hexadecanoyl HSL) were reduced, while shorter lipid conjugates (e.g.
366 *N*-tetradecanoyl- and *N*-pentadecanoyl HSL) were enriched. Changes in fatty amides were
367 associated with both *clsA* and *clsB* deletions, with many metabolites showing opposing trends
368 between mutant strains. Levels of several *N*-acyl amides were affected by both *clsA* and *clsB*
369 deletion, including *N*-hexadecyl-L-hydroxyproline, *N*-(3-hydroxy-14-methyldecanoyl) glycine, *N*-
370 palmitoyl threonine, and *N*-stearoyl tryptophan. Some *N*-acyl amides showed gene specific
371 changes such as *N*-(3-hydroxy-1-oxodecanoyl) glycine, which was primarily affected by *clsA*
372 deletion, and *N*-palmitoyl GABA, which was impacted by *clsB* deletion (Fig. 8F). *N*-acyl amides
373 may serve as additional carbon sources and/or signaling molecules between bacteria or to the
374 host, such as through G-protein coupled receptors (GPCRs) (80, 81). Molecular network analysis
375 identified *N*-acyl amides in larger clusters of chemically similar but unannotated metabolites,
376 suggesting that *cls* modifications may lead to larger global metabolomic shifts (Fig. S9). These
377 findings demonstrate that cardiolipin synthases play essential non-redundant roles in maintaining
378 metabolic homeostasis in *B. fragilis* P207.
379

380 **DISCUSSION**

381 In this study, we demonstrate that *B. fragilis* P207 has two functionally non-redundant
382 cardiolipin synthases, which we named ClsA and ClsB. Deleting either gene leads to distinct
383 defects in *B. fragilis* fitness under stress, with the loss of *clsB* generally being more detrimental
384 than *clsA* (Fig. 9). We note that *clsA* deletion results in elevated *clsB* expression, which may
385 partially compensate for and minimize the impact of its loss. We present evidence that ClsA and
386 ClsB synthesize cardiolipin species that differ in acyl chain length and unsaturation levels,

387 suggesting that each enzyme has unique substrate specificity and contributes distinct lipids to the
388 membrane. Furthermore, loss of either enzyme has knock-off effects on diverse cellular metabolic
389 processes.

390 This study is significant for several reasons. First, we offer an approach that integrates
391 metallomics-, lipidomics-, metabolomics-, and classical genetics-based techniques to investigate
392 cardiolipin synthase function. We employ tandem mass spectrometry to assess how *cls* deletion
393 affects the lipid composition of the *B. fragilis* envelope. To our knowledge, previous studies have
394 not leveraged high-resolution mass detection to differentiate the specific lipid species produced
395 by individual Cls proteins (26, 31, 41, 42, 82). While some have used MS/MS to characterize
396 membranes of diverse taxa, including *Bacteroides*, these approaches have not been applied to
397 strains with deletion of individual *cls* genes, limiting the identification of products associated with
398 each enzyme (76, 77, 83-86). By combining genetic and analytical approaches, we distinguish
399 the unique contributions of each Cls to the cardiolipin pool and intracellular ion gradient
400 homeostasis. Second, we provide functional characterization of *cls* genes in the *Bacteroides*
401 taxonomic group, particularly genes from a novel clinical isolate from the IBD gut. As important
402 members of the human gut ecosystem, *Bacteroides* species play key roles in microbiota
403 metabolism and host immune health (46). Understanding how these microbes regulate membrane
404 composition and homeostasis is essential for understanding their fitness in the context of the gut.
405 Future research should continue to explore cardiolipin biosynthesis in these organisms,
406 particularly in *B. thetaiotaomicron*, which possesses an additional *cls* not found in most other
407 *Bacteroides* species.

408 Due to the high diversity of bacterial *cls* genes, we struggled with the best approach to
409 name the *Bacteroides* group *cls* homologs (34, 82, 87, 88). While new letter codes (e.g. *clsX* or
410 *clsN*) might help distinguish *cls* gene diversity across bacteria, this naming scheme might have
411 become onerous upon characterization of other homologs. We therefore decided on the naming

412 conventions used for *E. coli cls* and other taxa, acknowledging that *cls* homologs across different
413 bacterial phyla may have distinct functional roles (89, 90).

414 The *B. fragilis cls* genes have some similarity to *E. coli clsA* and *clsB* as the genes from
415 both taxa have strong alignment with cardiolipin synthase domain models. However, at the amino
416 acid sequence level, no clear phylogenetic relationship exists between these homologs. In each
417 taxon, the ClsA homolog is predicted to have two N-terminal transmembrane helices. While these
418 domains in ClsA are thought to be cleaved post-translationally in *E. coli*, it is likely that this does
419 not occur in *Bacillus subtilis* (26, 90). Therefore, the functional consequences of these putative
420 transmembrane domains in *B. fragilis* remain unknown, particularly their role in the cellular
421 localization of these enzymes (90, 91). In addition, across these two taxa, the *cls* expression
422 profiles are distinct. *E. coli* relies almost exclusively on *clsA* during log phase, and expression of
423 *clsB* and *clsC* is largely limited to the stationary phase (26, 31, 41, 42). Under our growth
424 conditions, *B. fragilis* expresses both *cls* genes during log phase, with *clsA* expression further
425 enhanced during stationary phase. To determine if the two *B. fragilis* Cls have overlapping
426 enzymatic activities with the Cls of these other taxa, comparative biochemical analysis of the lipid
427 products produced by the Cls homologs of each species is needed.

428 Maintaining ion gradients across membranes is essential for bacterial survival, as these
429 gradients provide a reservoir of potential energy. The loss of cardiolipin biosynthesis under non-
430 stressed conditions largely does not affect ion homeostasis, as seen in our *B. fragilis* metallomic
431 studies. Bacteria generally tightly regulate intracellular K^+ content due to its physiological
432 importance, with some adjusting it by several fold depending on extracellular conditions (24, 92).
433 For example, *B. subtilis* and *E. coli* both increase intracellular K^+ levels in response to elevated
434 osmolarity (93, 94). However, *S. aureus* does not modulate K^+ content in this manner (95). While
435 one might expect ion gradient perturbations given previous work showing improved membrane
436 stability with the presence of cardiolipin (88, 96, 97), the resilience of intracellular K^+ and Na^+
437 levels in the absence of cardiolipin suggests that otherwise unperturbed cells maintain membrane

438 integrity. Even if loss of cardiolipin changed the inherent membrane permeability of either K^+ or
439 Na^+, our data indicate that *B. fragilis* leverages membrane remodeling and several compensatory
440 ion shuttling systems to achieve and maintain intracellular homeostasis (Fig. 5C-D) (24, 92, 98-
441 103).

442 While *B. fragilis clsA* is not essential and may even diminish fitness during selective ion
443 permeabilization, both *cls* genes are beneficial when the bacterium faces broader membrane
444 stress conditions. Although unlikely, the absence of ClsA-associated cardiolipins in the Δ*clsA*
445 strain may provide stress resistance by impairing ionophore translocation across the membrane
446 (59, 104, 105). Our favored hypothesis is that Δ*clsA*-dependent membrane remodeling enhances
447 resilience to ion gradient loss, possibly through altered membrane protein or lipid function. Beyond
448 general effects like membrane fluidity, cardiolipins can influence bacterial physiology through
449 multiple pathways. For example, some proteins that influence cell shape and cell division, such
450 as the actin homolog MreB, rely on cardiolipin for proper folding at the membrane (106, 107).
451 Interactions of cardiolipin with membrane-bound or membrane-associated cell division/shape
452 proteins may also underlie our observation that the loss of cardiolipin biosynthesis results in *B.*
453 *fragilis* cell shape defects (60-66). The cls-specific cell size effects may be shaped by
454 asymmetrical distribution of cardiolipin species across inner and outer leaflets of the inner
455 membrane as well as inner leaflet of the outer membrane (16, 108-110).

456 The catalytic products of *B. fragilis* ClsA and ClsB, as inferred from our lipidomics data,
457 have distinct acyl chain lengths and unsaturation levels. In response to environmental changes,
458 bacteria can adjust these lipid properties, which are key factors influencing membrane fluidity and
459 permeability (111). For example, under conditions that increase membrane rigidity, such as lower
460 temperature or high pressure, microbes increase the abundance of highly unsaturated fatty acids
461 to restore membrane fluidity (112, 113). Exposure to membrane destabilizing agents, such as
462 alcohols, can result in decreased acyl chain unsaturation (114). Exposure to phenols, which can
463 also disrupt membranes, cause some anaerobes to increase their membrane fluidity by

464 incorporating fatty acids with trans-double bonds (115). Although *B. fragilis* apparently lacks
465 enzymes required for this particular mechanism of introducing double bonds, phylogenetically
466 diverse bacteria have other regulatory mechanisms for the introduction of double bonds into acyl
467 chains already present in the membrane (116, 117). Having two unique pools of cardiolipins with
468 corresponding membrane lipids that respond to cardiolipin fluctuations, such as hexosylceramide
469 for ClsA and *N*-acyl glycylserine for ClsB, would provide bacteria like *B. fragilis* with greater
470 adaptability in the face of diverse selective pressures in the gut.

471 The distinct metabolomic alterations observed in *B. fragilis* ClsA and ClsB mutants
472 underscore the non-redundant and critical roles of cardiolipin synthases in bacterial metabolic
473 homeostasis. Our results demonstrate that loss of either ClsA or ClsB leads to unique changes in
474 the abundance of key lipid and non-lipid metabolites. These changes likely reflect the broader
475 disruptions in membrane composition and cellular signaling, as well as shifts in central metabolic
476 pathways. Importantly, the non-additive nature of the double mutant phenotype suggests that ClsA
477 and ClsB may influence partially overlapping yet distinct biosynthetic networks. The pronounced
478 depletion and enrichment of specific metabolites, such as lipid-conjugated HSLs and *N*-acyl
479 amides, further indicates that cardiolipin synthase activity influences both membrane structure
480 and intercellular communication. Given the essential role of membrane integrity and metabolic
481 adaptability in bacterial survival within the gut environment, these findings suggest that ClsA and
482 ClsB are pivotal for the ecological fitness of *B. fragilis*.

483 In summary, *B. fragilis* relies on cardiolipin synthases to maintain barrier integrity against
484 diverse stresses that it encounters in the gut, such as bile acids and osmotic variation. However,
485 much remains to be discovered regarding *B. fragilis* Cls-mediated physiology, including protein
486 domain function, cellular localization, and the mechanism by which each enzyme produces
487 distinct cardiolipins. Furthermore, the overlapping, yet possibly distinct, functional roles that this
488 diverse enzyme class plays across the prokaryotic tree of life is ripe with potential. The data we
489 present here serve as a foundation for a deeper understanding of *B. fragilis* physiology specifically

490 as well as that of the Bacteroidota generally, potentially leading to the engineering of probiotic gut
491 species with improved gut fitness and therapeutic outcomes.
492

493 **METHODS (see supplemental methods for additional detail)**

494 ***Bacterial Growth and Strains***

495 *Strain generation*

496 *E. coli* strains were grown aerobically at 37˚ C in Miller LB broth. As appropriate, E. coli
497 cultures were supplemented with filter-sterilized 300 μM diaminopimelic acid (Sigma-Aldrich) to
498 grow auxotrophic strains and/or 100 μg/ml carbenicillin to select for plasmid containing cells. All
499 *B. fragilis* strains were grown in supplemented brain heart infusion (BHIS) medium. As
500 appropriate, cultures were supplemented with 5 μg/mL erythromycin for vector selection, 100
501 ng/mL anhydrotetracycline (aTC) for inducible ssbfe1 counter-selection (118) and 50 ng/mL aTC
502 to induce expression from aTC-inducible complementation vectors (118). *B. fragilis* strains were
503 manipulated aerobically and grown at 37˚C in an anaerobic chamber (Coy Laboratory Products)
504 filled with 5% CO_2, 2.5% hydrogen and 92.5% nitrogen.

505 Mutant strains were generated by allelic exchange using modified vectors described
506 previously (118). For conjugation into *B. fragilis* P207, plasmids were transformed into the donor
507 *E. coli* strain WM3064. Allele exchange was conducted as previously described (118). The Δ*clsA*
508 mutant (lacking ptos_000612) was complemented by integration of an aTC-inducible *clsA*
509 construct. The Δ*clsB* mutant (lacking ptos_003215) was complemented by integration of *clsB*
510 under the control of a constitutive *Bacteroides* promoter (P_{rpoD}, bt_1311/BT_RS06635).
511 Complementation constructs were integrated into the chromosome at the *att* site using an intN1
512 integrase (119). Primers, vectors, and strains are listed in Tables S1–3, respectively.
513

514 ***Cls conservation analysis***

515 *Alignment.* The *B. fragilis* P207 ClsA and ClsB gene and protein sequences, as well as *E.*
516 *coli* K-12 MG1655 (NC_000913) ClsA, ClsB, and ClsC were aligned using default settings of the
517 Geneious alignment algorithm (Geneious Prime 2024) (51, 52).

518 *DeepTMHMM*. The ClsA and ClsB amino acid sequences from *B. fragilis* P207 and *E. coli*
519 K-12 MG1655 were uploaded to DeepTMHMM (v. 1.0.42, https://dtu.biolib.com/DeepTMHMM) to
520 predict transmembrane domains (120).

521 *Inter-Phylum Tree.* Representative taxa were selected from the top five phyla in the human
522 gut (metadata listed in Table S3) (121, 122). Annotated *cls* genes were obtained from genomes
523 on NCBI and protein aligned in Geneious. One genome per species was used, aside from the two
524 *B. fragilis* strains. The phylogenetic tree was reconstructed using neighbor-end joining via
525 Geneious and then visualized using R.

526 *Intra*-Bacteroides *Tree.* TIGR04265 domains in *B. fragilis* ClsA and ClsB were identified
527 using the conserved domain database of NCBI (123). *Bacteroides* protein sequences containing
528 this domain were obtained by querying the Interpro database. Alignment, tree reconstruction, and
529 tree visualization were performed as with the inter-phylum tree, except that *E. coli* K-12 MG1655
530 ClsA was specified as an outgroup.

531 *Genomic Neighborhoods.* WebFlags2 was used to query genomic neighborhoods around
532 *B. fragilis* P207 *clsA* and *clsB* genes (124).

533

534 ***Growth curve assays***

535 Stationary phase *B. fragilis* strain cultures were back-diluted to an optical density at 600
536 nm (OD_{600}) of 0.05 and grown to OD_{600} 0.3 in the presence of 50 ng/mL aTC inducer. Each strain
537 was then diluted again to 0.025–0.05 for growth curves in a 96-well plate format. OD_{600} was
538 measured with a Tecan Infinite M Nano plate reader (Tecan, Männedorf, Switzerland) for 24 h.
539 Three biological replicates, each in technical triplicate, were performed for each growth condition.

540 To expose cells to stress conditions, BHIS medium was prepared as above but modified.
541 For pH assays, cells were pelleted and then resuspended in aTC-containing BHIS medium
542 adjusted to the appropriate pH. For deoxycholate and SDS assays, 0.01% (w/v) deoxycholate
543 (Sigma) or 0.002% (w/v) SDS (Lab Scientific) was added to cultures from filter-sterilized 1% (w/v)
544 stocks dissolved in UltraPure water. For Na^+ and K^+ assays, NaCl (Fisher Scientific) and KCl
545 (Fisher Scientific) were dissolved to a 4× concentration of each cation in BHIS medium and then
546 filter sterilized before being added to cells to yield the final concentration of cells and cation (i.e.,
547 300 mM). To determine how much additional NaCl or KCl to add, the average Na^+ and K^+ content
548 of our BHIS medium was determined using ICP-MS (see below for methods), yielding 130 mM
549 for Na^+ and 33 mM for K^+ (Table S5). For ionophore assays, a concentrated ionophore (monensin
550 A or nigericin; Sigma-Aldrich) was added to cultures to yield final concentrations of 0.8 µg/mL
551 monensin A or 0.1 µg/mL nigericin, with equivalent volumes of ethanol added to non-treated
552 conditions as a vehicle control. We calculated maximum OD600 and doubling time using R
553 (ipolygrowth; see supplemental methods) (125).
554
555 ***Microscopy***
556 *B. fragilis* P207 cell cultures were grown overnight under antibiotic selection and then
557 back-diluted into medium containing inducer (aTC) without antibiotic selection to reach log-phase
558 growth. All cultures were removed from the 37ºC incubator but were maintained under anaerobic
559 conditions, with only two or three cultures removed for microscopy at a time. Cells were visualized
560 by phase-contrast microscopy on a Leica DMI6000 B inverted microscope with a Hamamatsu
561 ORCA-R2 10600 camera with a 63× Plan Apo objective (126). Each strain was visualized on four
562 different days to generate four biological replicates. The two images per replicate from each
563 strain/day were chosen for analysis. Chosen images were processed using the MicrobeJ plugin
564 (v. 5.13I) cell size analysis software in Fiji (v. 1.54k) (127). Called cells were manually curated and

565 resulting cell lengths and widths were exported and analyzed in R to calculate cell volume and
566 Epanechnikov kernel densities.
567
568 ***Gene expression assays***
569 *Stress condition exposure*: For comparison of *cls* gene expression at log and stationary
570 phases, *B. fragilis* WT, Δ*clsA* and Δ*clsB* strain log phase cultures were back diluted to an OD_{600}
571 of 0.05 without inducer. Two and 24 h later, cell samples were pelleted and resuspended in 1 mL
572 of Trizol (Invitrogen). For acute toxicity assays, back-diluted WT *B. fragilis* cultures that reached
573 OD_{600} ~0.3–0.5 were exposed to a specified condition (i.e., pH, SDS, deoxycholate, K^+, monensin
574 A, or nigericin, as described for the growth assays) and incubated for 20 min before cell sample
575 collection.
576 *RNA extraction*: RNA was extracted as described previously (51). RNeasy Extraction Kit
577 (Qiagen) was used to treat samples with Turbo DNase (Invitrogen) using the manufacturers
578 protocol.
579 *RT-qPCR*: Samples were run in technical triplicate. *Ct* values were determined using a
580 QuantStudio5 (Applied Biosystems) instrument and a Luna One-Step RT-qPCR kit (NEB) for
581 target genes in each sample (51). Using *B. fragilis dnaN* (ptos_002600, encoding DNA
582 polymerase subunit beta) as a normalization gene.
583
584 ***Inductively coupled plasma mass spectrometry***
585 Log phase cells were removed from the anaerobic chamber for sample collection. If
586 exposed to a stress, cells were incubated for 20 min aerobically at room temperature with either
587 0.01% (w/v) deoxycholate, 0.8 µg/mL monensin A or 0.1 µg/mL nigericin. Cultures were spiked
588 with gadolinium-DOTA (Gd-DOTA, Macrocyclics) to a final concentration of 40 µM. Washing cells,
589 even with the BHIS medium cells were grown in, perturbs intracellular concentrations of small

590 alkali metals like Na^+ and K^+ making quantification difficult (Fig. S5A). Using a Gd-DOTA spike
591 enabled us to remove washing steps in the ICP-MS sample preparation process (128, 129).
592 For the wash experiment, wash condition cells were washed twice with either 250 mM
593 sucrose or BHIS media. Then, unwashed cells (i.e., no previous centrifugation) and resuspended
594 washed cells were transferred to a metal-free tube, given a Gd-DOTA spike to 40 μM, and then
595 pelleted. For *cls* and treatment comparison experiments, cells were unwashed.
596 Weighed cell pellets and supernatant were dried overnight, then digested using 70% HNO_2
597 acid, before diluting to 3% nitric acid. All standards, blanks, and ICP-MS samples were prepared
598 using ultra-trace metal grade nitric acid (70%, Fisher), ultrapure water (Millipore), metal free
599 polypropylene conical tubes (15 and 50 mL, Labcon), and trace metal grade pipette tips (Labcon).
600 All solutions were weighed for accurate elemental determination using the XSR205 DU semi-
601 analytical balance (Mettler Toledo).
602 Samples were analyzed using an Agilent 8900 Triple Quadrupole ICP-MS (Agilent
603 Technologies). To prepare ICP-MS standards, the multi element standard IV-65024 (Inorganic
604 Ventures) was diluted with 3% (v/v) nitric acid in ultrapure water. Internal standardization was
605 accomplished inline using a 200 ppb internal standard solution in 3% (v/v) nitric acid in ultrapure
606 water (IV-ICPMS-71D, Inorganic Ventures). The isotopes selected for analysis were ^{23}Na, ^{31}P, ^{32}S,
607 ^{39}K and ^{157}Gd with ^{45}Sc, ^{89}Y, ^{115}In, and ^{159}Tb used for internal standardization. For accurate
608 quantification of ^{31}P and ^{32}S, these isotopes were measured in the oxygen mode. To quantify
609 intracellular elemental concentration, the average strain-specific cell volume was determined and
610 then the molar concentration calculated for each element from the number of atoms per cell. The
611 ΔmM concentrations were calculated by subtracting the concentration of an element in the
612 medium from that in the intracellular space.
613
614 ***Lipidomics assays***

615 WT, Δ*clsA*, Δ*clsB*, and Δ*clsA* Δ*clsB* strains were backdiluted, grown to OD_{600} 0.7, and then
616 submitted on dry ice to the University of Tennessee-Knoxville Biological and Small Molecule Mass
617 Spectrometry Core (BSMMSC; RRID: SCR_021368) for targeted lipidomic analysis of membrane
618 lipids. Lipids were extracted as previously described (see supplemental methods for details) (130,
619 131). The lipidomic analyses were performed using a previously validated method (131) on an
620 ultra high performance liquid chromatography system coupled to a high resolution mass
621 spectrometer (UHPLC-HRMS). The chromatographic separations were carried out using
622 Vanquish Horizon LC system (Thermo Scientific) and reversed phase separations as described
623 previously (131). The eluent was introduced to an Exploris 120 mass spectrometer (Thermo
624 Scientific) via electrospray ionization for high resolution analysis. Following the analysis, the lipids
625 were annotated and the peak area integrated using MS-DIAL (132-135). Peak area for a
626 metabolite was first normalized to the optical density of a sample, then relative lipid abundance
627 was determined by normalizing to the total peak area of all lipids detected in each
628 UHPLC−MS/HRMS mode (i.e., positive versus negative). Elastic net regression performed using
629 the glmnet R package (136, 137).
630
631 ***Metabolomic assays***
632 WT, Δ*clsA*, Δ*clsB*, and Δ*clsA* Δ*clsB* strains were grown in 50mL BHIS medium and
633 metabolites were extracted with ethyl acetate (see supplemental methods for details). Untargeted
634 metabolomics data was acquired using a Bruker timsTOF Pro2 (Bruker-Daltonics, Billerica, MA,
635 USA) coupled to an Agilent 1290 Infinity II Bio UHPLC (Agilent, Santa Clara, CA, USA). The
636 chromatographic separations were carried out using an Acquity UPLC HSST3 column (2.1 x
637 150mm, 1.8 μM) (see supplemental methods for details). Following data acquisition, mass
638 spectrometry (MS) data were pre-processed using Bruker MetaboScape® version 9.0.1 (Bruker-
639 Daltonics, Billerica, MA, USA) and filtered using mpactR (see supplemental methods for details)
640 (138). Peak intensity for each metabolite was normalized to the total peak intensity of all features

641 detected in the sample. Molecular networking was generated as previously described (139) using
642 GNPS2: Global Natural Products Social Molecular Networking 2 (http://gnps2.org/). A minimum
643 cosine similarity score of 0.7 with at least six matching peaks, parent mass tolerance of 2 Da, and
644 fragment ion tolerance 0.5 Da were selected to generate consensus spectra. Files were imported
645 into CytoScape 3.10.3 and nodes were arranged with yFiles organic layout plugin (140). Pathway
646 analysis was performed with MetaboAnalyst 6.0 functional analysis [LC-MS] module (141). A
647 formatted peak intensity table was uploaded to the web server (https://metaboanalyst.ca), then
648 normalized by sum and log transformed. Default setting of 5.0 ppm mass tolerance, mummichog
649 algorithm v2.0 with p-value cutoff of 0.0005, against the lipid and non-lipid pathway libraries with
650 at least 3 entries in each pathway. Metabolites from enriched pathways were plotted using R
651 (v4.5.0).
652
653
654 ***Data analysis and reproducibility***
655 All data analyses were performed using R (v4.3.3 unless otherwise specified) and several
656 packages (125, 136, 137, 142-164). Code used and original datasets for all data analysis and
657 figure generation, except for the WebFlags neighborhoods, is published on GitHub
658 (https://github.com/mschnizlein/bfrag_cardiolipin). Lipidomics data alongside appropriate
659 metadata were deposited on MetaboLights (MTBLS11891
660 www.ebi.ac.uk/metabolights/MTBLS11891) (165). Untargeted metabolomics were deposited to
661 MassIVE (https://massive.ucsd.edu) (deposit in progress at time of submission).
662
663 **Acknowledgements**

664 We would like to thank the Biological and Small Molecule Mass Spectrometry Core (BSMMSC)
665 at the University of Tennessee-Knoxville and the Q-Beam Center at Michigan State University for

their work processing and analyzing samples for lipid and elemental analyses, respectively. We thank Drs. Kiwon Ok, Keith MacRenaris and Aaron Sue from the O'Halloran Lab for their advice on using the ICP-MS an analyzing output. We also would like to thank the entire Crosson Lab for their advice as the project progressed, particularly Dr. Melene Alakavuklar for her feedback on this manuscript and figure presentation, respectively. We used Biorender to generate the model presented in Figure 9. We thank two undergrads who piloted several experiments: Damone Charleston and Timothy Baldwin. We thank Kathryn McBride for strain culturing in the Balunas Lab. *E. coli* strain WM3064 was a gift from William Metcalf at UIUC. Work on this project in the S.C. lab was supported in part by NIDDK (RC2DK122394) and NIGMS (R35GM131762), in the T.V.O lab by NIGMS (P41GM135018), and in the M.J.B. lab by NCI (U01CA264071).

677 **REFERENCES**

678 1. Schnizlein MK, Young VB. 2022. Capturing the environment of the *Clostridioides difficile*
679 infection cycle. Nature Reviews Gastroenterology & Hepatology 19:508-520.
680 2. Shortt C, Hasselwander O, Meynier A, Nauta A, Fernández EN, Putz P, Rowland I,
681 Swann J, Türk J, Vermeiren J, Antoine J-M. 2018. Systematic review of the effects of the
682 intestinal microbiota on selected nutrients and non-nutrients. European Journal of
683 Nutrition 57:25-49.
684 3. Kern L, Abdeen SK, Kolodziejczyk AA, Elinav E. 2021. Commensal inter-bacterial
685 interactions shaping the microbiota. Current Opinion in Microbiology 63:158-171.
686 4. Runge S, Rosshart SP. 2021. The mammalian metaorganism: A holistic view on how
687 microbes of all kingdoms and niches shape local and systemic immunity. Frontiers in
688 Immunology 12.
689 5. He X, McLean JS, Guo L, Lux R, Shi W. 2014. The social structure of microbial
690 community involved in colonization resistance. ISME J 8:564-574.
691 6. Wennerström H, Oliveberg M. 2022. On the osmotic pressure of cells. QRB Discovery
692 3:e12.
693 7. Denyer SP, Maillard JY. 2002. Cellular impermeability and uptake of biocides and
694 antibiotics in Gram-negative bacteria. Journal of Applied Microbiology 92:35S-45S.
695 8. Zhang Y-M, Rock CO. 2008. Membrane lipid homeostasis in bacteria. Nature Reviews
696 Microbiology 6:222-233.
697 9. Strahl H, Errington J. 2017. Bacterial membranes: Structure, domains, and function.
698 Annual Review of Microbiology 71:519-538.
699 10. Sohlenkamp C, Geiger O. 2015. Bacterial membrane lipids: Diversity in structures and
700 pathways. FEMS Microbiology Reviews 40:133-159.
701 11. Blevins MS, James VK, Herrera CM, Purcell AB, Trent MS, Brodbelt JS. 2020.
702 Unsaturation elements and other modifications of phospholipids in bacteria: New insight
703 from ultraviolet photodissociation mass spectrometry. Analytical Chemistry 92:9146-
704 9155.
705 12. Roy H, Dare K, Ibba M. 2009. Adaptation of the bacterial membrane to changing
706 environments using aminoacylated phospholipids. Molecular Microbiology 71:547-550.
707 13. Cox E, Michalak A, Pagentine S, Seaton P, Pokorny A. 2014. Lysylated phospholipids
708 stabilize models of bacterial lipid bilayers and protect against antimicrobial peptides.
709 Biochimica et Biophysica Acta (BBA) - Biomembranes 1838:2198-2204.
710 14. Donohue TJ, Cain BD, Kaplan S. 1982. Alterations in the phospholipid composition of
711 *Rhodopseudomonas sphaeroides* and other bacteria induced by Tris. Journal of
712 Bacteriology 152:595-606.
713 15. Lin T-Y, Weibel DB. 2016. Organization and function of anionic phospholipids in bacteria.
714 Applied Microbiology and Biotechnology 100:4255-4267.
715 16. Bogdanov M, Pyrshev K, Yesylevskyy S, Ryabichko S, Boiko V, Ivanchenko P, Kiyamova
716 R, Guan Z, Ramseyer C, Dowhan W. 2020. Phospholipid distribution in the cytoplasmic
717 membrane of Gram-negative bacteria is highly asymmetric, dynamic, and cell shape-
718 dependent. Science Advances 6:eaaz6333.
719 17. Poolman B. 2023. Physicochemical homeostasis in bacteria. FEMS Microbiology
720 Reviews 47.
721 18. Zharova TV, Grivennikova VG, Borisov VB. 2023. $F_1 \cdot F_o$ ATP synthase/ATPase:
722 Contemporary view on unidirectional catalysis. International Journal of Molecular
723 Sciences 24:5417.
724 19. Haddock BA, Jones CW. 1977. Bacterial respiration. Bacteriol Rev 41:47-99.
725 20. Lu Z, Imlay JA. 2021. When anaerobes encounter oxygen: Mechanisms of oxygen
726 toxicity, tolerance and defence. Nature Reviews Microbiology 19:774-785.

727 21. Ito T, Gallegos R, Matano LM, Butler NL, Hantman N, Kaili M, Coyne MJ, Comstock LE,
728 Malamy MH, Barquera B. 2020. Genetic and biochemical analysis of anaerobic
729 respiration in *Bacteroides fragilis* and its importance *in vivo*. mBio 11:e03238-19.
730 22. Butler NL, Ito T, Foreman S, Morgan JE, Zagorevsky D, Malamy MH, Comstock LE,
731 Barquera B. 2023. *Bacteroides fragilis* maintains concurrent capability for anaerobic and
732 nanaerobic respiration. Journal of Bacteriology 205:e00389-22.
733 23. Beagle SD, Lockless SW. 2021. Unappreciated roles for K^+ channels in bacterial
734 physiology. Trends in Microbiology 29:942-950.
735 24. Stautz J, Hellmich Y, Fuss MF, Silberberg JM, Devlin JR, Stockbridge RB, Hänelt I. 2021.
736 Molecular mechanisms for bacterial potassium homeostasis. Journal of Molecular
737 Biology 433:166968.
738 25. Schlame M. 2008. *Thematic Review Series: Glycerolipids.* Cardiolipin synthesis for the
739 assembly of bacterial and mitochondrial membranes. Journal of Lipid Research 49:1607-
740 1620.
741 26. Tropp BE. 1997. Cardiolipin synthase from *Escherichia coli*. Biochimica et Biophysica
742 Acta (BBA) - Lipids and Lipid Metabolism 1348:192-200.
743 27. Pinkas D, Fišer R, Kozlík P, Dolejšová T, Hryzáková K, Konopásek I, Mikušová G. 2020.
744 *Bacillus subtilis* cardiolipin protects its own membrane against surfactin-induced
745 permeabilization. Biochimica et Biophysica Acta (BBA) - Biomembranes 1862:183405.
746 28. Chen Q-P, Li Q-T. 2001. Effect of cardiolipin on proton permeability of phospholipid
747 liposomes: The role of hydration at the lipid–water interface. Archives of Biochemistry
748 and Biophysics 389:201-206.
749 29. Domitin S, Puff N, Pilot-Storck F, Tiret L, Joubert F. 2025. Role of cardiolipin in proton
750 transmembrane flux and localization. Biophysical Journal 124:408-416.
751 30. Shibata A, Ikawa K, Shimooka T, Terada H. 1994. Significant stabilization of the
752 phosphatidylcholine bilayer structure by incorporation of small amounts of cardiolipin.
753 Biochimica et Biophysica Acta (BBA) - Biomembranes 1192:71-78.
754 31. Jeucken A, Helms JB, Brouwers JF. 2018. Cardiolipin synthases of *Escherichia coli* have
755 phospholipid class specific phospholipase D activity dependent on endogenous and
756 foreign phospholipids. Biochimica et Biophysica Acta (BBA) - Molecular and Cell Biology
757 of Lipids 1863:1345-1353.
758 32. Domitin S, Puff N, Pilot-Storck F, Tiret L, Joubert F. 2025. Role of cardiolipin in proton
759 transmembrane flux and localization. Biophys J 124:408-416.
760 33. Shibata A, Ikawa K, Shimooka T, Terada H. 1994. Significant stabilization of the
761 phosphatidylcholine bilayer structure by incorporation of small amounts of cardiolipin.
762 Biochim Biophys Acta 1192:71-8.
763 34. Yeo W-S, Dyzenhaus S, Torres VJ, Brinsmade SR, Bae T. 2023. Regulation of bacterial
764 two-component systems by cardiolipin. Infection and Immunity 91:e00046-23.
765 35. Ryabichko S, Ferreira VdM, Vitrac H, Kiyamova R, Dowhan W, Bogdanov M. 2020.
766 Cardiolipin is required *in vivo* for the stability of bacterial translocon and optimal
767 membrane protein translocation and insertion. Scientific Reports 10:6296.
768 36. Musatov A, Sedlák E. 2017. Role of cardiolipin in stability of integral membrane proteins.
769 Biochimie 142:102-111.
770 37. Hong Y, Muenzner J, Grimm SK, Pletneva EV. 2012. Origin of the conformational
771 heterogeneity of cardiolipin-bound cytochrome c. Journal of the American Chemical
772 Society 134:18713-18723.
773 38. Arias-Cartin R, Grimaldi S, Arnoux P, Guigliarelli B, Magalon A. 2012. Cardiolipin binding
774 in bacterial respiratory complexes: Structural and functional implications. Biochimica et
775 Biophysica Acta (BBA) - Bioenergetics 1817:1937-1949.

39. Planas-Iglesias J, Dwarakanath H, Mohammadyani D, Yanamala N, Kagan Valerian E, Klein-Seetharaman J. 2015. Cardiolipin interactions with proteins. Biophysical Journal 109:1282-1294.
40. Hirschberg CB, Kennedy EP. 1972. Mechanism of the enzymatic synthesis of cardiolipin in *Escherichia coli*. Proceedings of the National Academy of Sciences 69:648-651.
41. Tan BK, Bogdanov M, Zhao J, Dowhan W, Raetz CR, Guan Z. 2012. Discovery of a cardiolipin synthase utilizing phosphatidylethanolamine and phosphatidylglycerol as substrates. Proceedings of the National Academy of Sciences 109:16504-16509.
42. Guo D, Tropp BE. 2000. A second *Escherichia coli* protein with CL synthase activity. Biochimica et Biophysica Acta (BBA) - Molecular and Cell Biology of Lipids 1483:263-274.
43. Li C, Tan BK, Zhao J, Guan Z. 2016. *In Vivo* and *in Vitro* synthesis of phosphatidylglycerol by an *Escherichia coli* cardiolipin synthase. Journal of Biological Chemistry 291:25144-25153.
44. Homma H, Nojima S. 1982. Synthesis of various phospholipids from 2-acyl lysophospholipids by *Escherichia coli* extract. The Journal of Biochemistry 91:1103-1110.
45. Patrick S. 2022. A tale of two habitats: *Bacteroides fragilis*, a lethal pathogen and resident in the human gastrointestinal microbiome. Microbiology 168.
46. Wexler HM. 2007. *Bacteroides*: The good, the bad, and the nitty-gritty. Clin Microbiol Rev 20:593-621.
47. Tally FP, Stewart PR, Sutter VL, Rosenblatt JE. 1975. Oxygen tolerance of fresh clinical anaerobic bacteria. J Clin Microbiol 1:161-4.
48. Valguarnera E, Wardenburg JB. 2020. Good Gone Bad: One Toxin Away From Disease for Bacteroides fragilis. J Mol Biol 432:765-785.
49. Scott N, Whittle E, Jeraldo P, Chia N. 2022. A systemic review of the role of enterotoxic *Bacteroides fragilis* in colorectal cancer. Neoplasia 29:100797.
50. Sun F, Zhang Q, Zhao J, Zhang H, Zhai Q, Chen W. 2019. A potential species of next-generation probiotics? The dark and light sides of *Bacteroides fragilis* in health. Food Res Int 126:108590.
51. Fiebig A, Schnizlein MK, Pena-Rivera S, Trigodet F, Dubey AA, Hennessy MK, Basu A, Pott S, Dalal S, Rubin D, Sogin ML, Eren AM, Chang EB, Crosson S. 2024. Bile acid fitness determinants of a *Bacteroides fragilis* isolate from a human pouchitis patient. mBio 15:e02830-23.
52. Vineis JH, Ringus DL, Morrison HG, Delmont TO, Dalal S, Raffals LH, Antonopoulos DA, Rubin DT, Eren AM, Chang EB, Sogin ML. 2016. Patient-specific *Bacteroides* genome variants in pouchitis. mBio 7:e01713-16.
53. Akiyama S, Rai V, Rubin DT. 2021. Pouchitis in inflammatory bowel disease: a review of diagnosis, prognosis, and treatment. Intest Res 19:1-11.
54. Sitaraman R. 2013. Phospholipid catabolism by gut microbiota and the risk of cardiovascular disease. J Med Microbiol 62:948-950.
55. Romantsov T, Gonzalez K, Sahtout N, Culham DE, Coumoundouros C, Garner J, Kerr CH, Chang L, Turner RJ, Wood JM. 2018. Cardiolipin synthase A colocalizes with cardiolipin and osmosensing transporter ProP at the poles of *Escherichia coli* cells. Molecular Microbiology 107:623-638.
56. Quigley BR, Tropp BE. 2009. *E. coli* cardiolipin synthase: Function of N-terminal conserved residues. Biochimica et Biophysica Acta (BBA) - Biomembranes 1788:2107-2113.
57. Antonenko YN, Yaguzhinsky LS. 1988. The ion selectivity of nonelectrogenic ionophores measured on a bilayer lipid membrane: Nigericin, monensin, A23187 and lasalocid A. Biochim Biophys Acta 938:125-30.

58. Li J, Ding L, Wang E, Dong S. 1996. The ion selectivity of monensin incorporated phospholipid/alkanethiol bilayers. Journal of Electroanalytical Chemistry 414:17-21.
59. Łowicki D, Huczyński A. 2013. Structure and antimicrobial properties of monensin A and its derivatives: Summary of the achievements. BioMed Research International 2013:742149.
60. Lin T-Y, Gross William S, Auer George K, Weibel Douglas B. 2019. Cardiolipin alters *Rhodobacter sphaeroides* cell shape by affecting peptidoglycan precursor biosynthesis. mBio 10.
61. Elías-Wolff F, Lindén M, Lyubartsev AP, Brandt EG. 2019. Curvature sensing by cardiolipin in simulated buckled membranes. Soft Matter 15:792-802.
62. Luchini A, Cavasso D, Radulescu A, D'Errico G, Paduano L, Vitiello G. 2021. Structural organization of cardiolipin-containing vesicles as models of the bacterial cytoplasmic membrane. Langmuir 37:8508-8516.
63. Labajová N, Baranova N, Jurásek M, Vácha R, Loose M, Barák I. 2021. Cardiolipin-containing lipid membranes attract the bacterial cell division protein DivIVA. International Journal of Molecular Sciences 22:8350.
64. Renner LD, Weibel DB. 2011. Cardiolipin microdomains localize to negatively curved regions of *Escherichia coli* membranes. Proceedings of the National Academy of Sciences 108:6264-6269.
65. Huang KC, Mukhopadhyay R, Wingreen NS. 2006. A curvature-mediated mechanism for localization of lipids to bacterial poles. PLOS Computational Biology 2:e151.
66. Bailey BWA, Stansfeld PJ. 2024. The bacterial cytoskeleton alters the cell membrane in molecular dynamics simulations. Biophysical Journal 123:374a.
67. Rowlett VW, Mallampalli VKPS, Karlstaedt A, Dowhan W, Taegtmeyer H, Margolin W, Vitrac H. 2017. Impact of membrane phospholipid alterations in *Escherichia coli* on cellular function and bacterial stress adaptation. Journal of Bacteriology 199:10.1128/jb.00849-16.
68. Duncan AL, Robinson AJ, Walker JE. 2016. Cardiolipin binds selectively but transiently to conserved lysine residues in the rotor of metazoan ATP synthases. Proc Natl Acad Sci U S A 113:8687-92.
69. Mehdipour AR, Hummer G. 2016. Cardiolipin puts the seal on ATP synthase. Proc Natl Acad Sci U S A 113:8568-70.
70. Shapiro JS, Chang H-C, Tatekoshi Y, Zhao Z, Waxali ZS, Hong BJ, Chen H, Geier JA, Bartom ET, De Jesus A, Nejad FK, Mahmoodzadeh A, Sato T, Ramos-Alonso L, Romero AM, Martinez-Pastor MT, Jiang S-C, Sah-Teli SK, Li L, Bentrem D, Lopaschuk G, Ben-Sahra I, O'Halloran TV, Shilatifard A, Puig S, Bergelson J, Koivunen P, Ardehali H. 2023. Iron drives anabolic metabolism through active histone demethylation and mTORC1. Nature Cell Biology 25:1478-1494.
71. Lane A, Gokhale A, Werner E, Roberts A, Freeman A, Roberts B, Faundez V. 2022. Sulfur- and phosphorus-standardized metal quantification of biological specimens using inductively coupled plasma mass spectrometry. STAR Protoc 3:101334.
72. Schaechter M, MaalØe O, Kjeldgaard NO. 1958. Dependency on medium and temperature of cell size and chemical composition during balanced growth of *Salmonella typhimurium*. Microbiology 19:592-606.
73. Kjeldgaard NO, MaalØe O, Schaechter M. 1958. The transition between different physiological states during balanced growth of *Salmonella typhimurium*. Microbiology 19:607-616.
74. Mulyukin AL, Sorokin VV, Loiko NG, Suzina NE, Duda VI, Vorob'eva EA, El'-Registan GI. 2002. Comparative study of the elemental composition of vegetative and resting microbial cells. Microbiology 71:31-40.

75. Sivakumar P, Fernández-Bravo A, Taleh L, Biddle JF, Melikechi N. 2015. Detection and classification of live and dead *Escherichia coli* by laser-induced breakdown spectroscopy. Astrobiology 15:144-153.
76. Sartorio Mariana G, Valguarnera E, Hsu F-F, Feldman Mario F. 2022. Lipidomics analysis of outer membrane vesicles and elucidation of the inositol phosphoceramide biosynthetic pathway in *Bacteroides thetaiotaomicron*. Microbiology Spectrum 10:e00634-21.
77. Ryan E, Gonzalez Pastor B, Gethings LA, Clarke DJ, Joyce SA. 2023. Lipidomic analysis reveals differences in *Bacteroides* species driven largely by plasmalogens, glycerophosphoinositols and certain sphingolipids. Metabolites 13:360.
78. Rizza V, Tucker Anne N, White David C. 1970. Lipids of *Bacteroides melaninogenicus*. Journal of Bacteriology 101:84-91.
79. Withers H, Swift S, Williams P. 2001. Quorum sensing as an integral component of gene regulatory networks in Gram-negative bacteria. Current Opinion in Microbiology 4:186-193.
80. Otaru N, Ye K, Mujezinovic D, Berchtold L, Constancias F, Cornejo FA, Krzystek A, de Wouters T, Braegger C, Lacroix C, Pugin B. 2021. GABA production by human intestinal Bacteroides spp.: Prevalence, regulation, and role in acid stress tolerance. Frontiers in Microbiology 12.
81. Cohen LJ, Kang HS, Chu J, Huang YH, Gordon EA, Reddy BV, Ternei MA, Craig JW, Brady SF. 2015. Functional metagenomic discovery of bacterial effectors in the human microbiome and isolation of commendamide, a GPCR G2A/132 agonist. Proc Natl Acad Sci U S A 112:E4825-34.
82. Koprivnjak T, Zhang D, Ernst CM, Peschel A, Nauseef WM, Weiss JP. 2011. Characterization of *Staphylococcus aureus* cardiolipin synthases 1 and 2 and their contribution to accumulation of cardiolipin in stationary phase and within phagocytes. Journal of Bacteriology 193:4134-4142.
83. Mirretta Barone C, Heaver SL, Gruber L, Zundel F, Vu DL, Ley RE. 2024. Spatially resolved lipidomics shows conditional transfer of lipids produced by Bacteroides thetaiotaomicron into the mouse gut. Cell Host & Microbe 32:1025-1036.e5.
84. An D, Na C, Bielawski J, Hannun YA, Kasper DL. 2011. Membrane sphingolipids as essential molecular signals for Bacteroides survival in the intestine. Proceedings of the National Academy of Sciences 108:4666-4671.
85. Frankfater CF, Sartorio MG, Valguarnera E, Feldman MF, Hsu F-F. 2023. Lipidome of the Bacteroides Genus Containing New Peptidolipid and Sphingolipid Families Revealed by Multiple-Stage Mass Spectrometry. Biochemistry 62:1160-1180.
86. Hines KM, Xu L. 2019. Lipidomic consequences of phospholipid synthesis defects in *Escherichia coli* revealed by HILIC-ion mobility-mass spectrometry. Chemistry and Physics of Lipids 219:15-22.
87. Czolkoss S, Fritz C, Hölzl G, Aktas M. 2016. Two distinct cardiolipin synthases operate in *Agrobacterium tumefaciens*. PLOS ONE 11:e0160373.
88. Tsai M, Ohniwa RL, Kato Y, Takeshita SL, Ohta T, Saito S, Hayashi H, Morikawa K. 2011. *Staphylococcus aureus* requires cardiolipin for survival under conditions of high salinity. BMC Microbiology 11:13.
89. Liu J, Ryabichko S, Bogdanov M, Fackelmayer OJ, Dowhan W, Krulwich TA. 2014. Cardiolipin is dispensable for oxidative phosphorylation and non-fermentative growth of alkaliphilic Bacillus pseudofirmus OF4. J Biol Chem 289:2960-71.
90. Kusaka J, Shuto S, Imai Y, Ishikawa K, Saito T, Natori K, Matsuoka S, Hara H, Matsumoto K. 2016. Septal localization by membrane targeting sequences and a conserved sequence essential for activity at the COOH-terminus of *Bacillus subtilis* cardiolipin synthase. Research in Microbiology 167:202-214.

91. Shibuya I, Yamagoe S, Miyazaki C, Matsuzaki H, Ohta A. 1985. Biosynthesis of novel acidic phospholipid analogs in *Escherichia coli*. Journal of Bacteriology 161:473-477.
92. Walderhaug MO, Dosch DC, Epstein W. 1987. Potassium Transport in Bacteria, p 85-130. *In* Rosen BP, Silver S (ed), Ion Transport in Prokaryotes doi:10.1016/B978-0-12-596935-2.50005-0. Academic Press.
93. Whatmore AM, Chudek JA, Reed RH. 1990. The effects of osmotic upshock on the intracellular solute pools of *Bacillus subtilis*. Microbiology 136:2527-2535.
94. Epstein W. 1986. Osmoregulation by potassium transport in *Escherichia coli*. FEMS Microbiology Reviews 2:73-78.
95. Christian JHB, Waltho JA. 1964. The composition of *Staphylococcus aureus* in relation to the water activity of the growth medium. Microbiology 35:205-213.
96. Jagannathan S. 1994. Characterization of proton and water permeability across model membrane vesicles and proteoliposomes. 9600672. Clemson University, South Carolina, USA.
97. Kato S, Tobe H, Matsubara H, Sawada M, Sasaki Y, Fukiya S, Morita N, Yokota A. 2019. The membrane phospholipid cardiolipin plays a pivotal role in bile acid adaptation by Lactobacillus gasseri JCM1131T. Biochimica et Biophysica Acta (BBA) - Molecular and Cell Biology of Lipids 1864:403-412.
98. Dimroth P. 1994. Bacterial sodium ion-coupled energetics. Antonie Van Leeuwenhoek 65:381-95.
99. Mulkidjanian AY, Dibrov P, Galperin MY. 2008. The past and present of sodium energetics: may the sodium-motive force be with you. Biochim Biophys Acta 1777:985-92.
100. Ren Q, Paulsen IT. 2009. Transport, Solute, p 529-544. *In* Schaechter M (ed), Encyclopedia of Microbiology (Third Edition) doi:10.1016/B978-012373944-5.00107-3. Academic Press, Oxford.
101. van de Vossenberg JL, Ubbink-Kok T, Elferink MG, Driessen AJ, Konings WN. 1995. Ion permeability of the cytoplasmic membrane limits the maximum growth temperature of bacteria and archaea. Mol Microbiol 18:925-32.
102. Deamer DW, Bramhall J. 1986. Permeability of lipid bilayers to water and ionic solutes. Chemistry and Physics of Lipids 40:167-188.
103. Hopfer U, Lehninger AL, Lennarz WJ. 1970. The effect of the polar moiety of lipids on the ion permeability of bilayer membranes. The Journal of Membrane Biology 2:41-58.
104. Russell JB. 1987. A proposed mechanism of monensin action in inhibiting ruminant bacterial growth: Effects on ion flux and proton motive force. Journal of Animal Science 64:1519-1525.
105. Guffanti AA, Davidson LF, Mann TM, Krulwich TA. 1979. Nigericin-induced death of an acidophilic bacterium. Microbiology 114:201-206.
106. Ouellette SP, Fisher-Marvin LA, Harpring M, Lee J, Rucks EA, Cox JV. 2022. Localized cardiolipin synthesis is required for the assembly of MreB during the polarized cell division of *Chlamydia trachomatis*. PLOS Pathogens 18:e1010836.
107. Kurita K, Kato F, Shiomi D. 2020. Alteration of membrane fluidity or phospholipid composition perturbs rotation of MreB complexes in *Escherichia coli*. Frontiers in Molecular Biosciences 7.
108. Dong H, Zhang Z, Tang X, Huang S, Li H, Peng B, Dong C. 2016. Structural insights into cardiolipin transfer from the Inner membrane to the outer membrane by PbgA in Gram-negative bacteria. Scientific Reports 6:30815-30815.
109. Bogdanov M. 2023. The power and challenge of lipid (a)symmetry across the membrane and cell. Emerging Topics in Life Sciences 7:1-6.

110. Bogdanov M. 2023. Renovating a double fence with or without notifying the next door and across the street neighbors: why the biogenic cytoplasmic membrane of Gram-negative bacteria display asymmetry? . Emerging Topics in Life Sciences 7:137-150.
111. Lande MB, Donovan JM, Zeidel ML. 1995. The relationship between membrane fluidity and permeabilities to water, solutes, ammonia, and protons. Journal of General Physiology 106:67-84.
112. Neidleman SL. 1987. Effects of temperature on lipid unsaturation. Biotechnology and Genetic Engineering Reviews 5:245-268.
113. Yano Y, Nakayama A, Ishihara K, Saito H. 1998. Adaptive changes in membrane lipids of barophilic bacteria in response to changes in growth pressure. Applied and Environmental Microbiology 64:479-485.
114. Huffer S, Clark ME, Ning JC, Blanch HW, Clark DS. 2011. Role of alcohols in growth, lipid composition, and membrane fluidity of yeasts, bacteria, and archaea. Applied and Environmental Microbiology 77:6400-6408.
115. Keweloh H, Heipieper HJ. 1996. Trans unsaturated fatty acids in bacteria. Lipids 31:129-137.
116. Altabe SG, Aguilar P, Caballero GM, de Mendoza D. 2003. The *Bacillus subtilis* acyl lipid desaturase is a delta5 desaturase. J Bacteriol 185:3228-31.
117. Schweizer HP, Choi K-H. 2011. *Pseudomonas aeruginosa* aerobic fatty acid desaturase DesB is important for virulence factor production. Archives of Microbiology 193:227-234.
118. García-Bayona L, Comstock LE. 2019. Streamlined genetic manipulation of diverse *Bacteroides* and *Parabacteroides* isolates from the human gut microbiota. mBio 10.
119. Rajeev L, Segall A, Gardner J. 2007. The *Bacteroides* NBU1 integrase performs a homology-independent strand exchange to form a holliday junction intermediate. J Biol Chem 282:31228-37.
120. Hallgren J, Tsirigos KD, Pedersen MD, Almagro Armenteros JJ, Marcatili P, Nielsen H, Krogh A, Winther O. 2022. DeepTMHMM predicts alpha and beta transmembrane proteins using deep neural networks. bioRxiv doi:10.1101/2022.04.08.487609:2022.04.08.487609.
121. Bäckhed F, Ley RE, Sonnenburg JL, Peterson DA, Gordon JI. 2005. Host-bacterial mutualism in the human intestine. Science 307:1915-1920.
122. Adak A, Khan MR. 2019. An insight into gut microbiota and its functionalities. Cellular and Molecular Life Sciences 76:473-493.
123. Lu S, Wang J, Chitsaz F, Derbyshire MK, Geer RC, Gonzales NR, Gwadz M, Hurwitz DI, Marchler GH, Song JS, Thanki N, Yamashita RA, Yang M, Zhang D, Zheng C, Lanczycki CJ, Marchler-Bauer A. 2020. CDD/SPARCLE: The conserved domain database in 2020. Nucleic Acids Res 48:D265-d268.
124. Saha CK, Sanches Pires R, Brolin H, Delannoy M, Atkinson GC. 2020. FlaGs and webFlaGs: Discovering novel biology through the analysis of gene neighbourhood conservation. Bioinformatics 37:1312-1314.
125. Wang J, Barger K. 2024. ipolygrowth: An R package to calculate individual growth curve parameters from bacterial time series data. Microbiology Resource Announcements 13:e00662-24.
126. McLaughlin M, Fiebig A, Crosson S. 2023. XRE transcription factors conserved in Caulobacter and φCbK modulate adhesin development and phage production. PLOS Genetics 19:e1011048.
127. Ducret A, Quardokus EM, Brun YV. 2016. MicrobeJ, a tool for high throughput bacterial cell detection and quantitative analysis. Nature Microbiology 1:16077.
128. Sakol N, Egawa A, Fujiwara T. 2020. Gadolinium complexes as contrast agent for cellular NMR spectroscopy. Int J Mol Sci 21:4042.

129. Aime S, Cabella C, Colombatto S, Geninatti Crich S, Gianolio E, Maggioni F. 2002. Insights into the use of paramagnetic Gd(III) complexes in MR-molecular imaging investigations. Journal of Magnetic Resonance Imaging 16:394-406.
130. Basso JTR, Jones KA, Jacobs KR, Christopher CJ, Fielland HB, Campagna SR, Buchan A. 2022. Growth Substrate and Prophage Induction Collectively Influence Metabolite and Lipid Profiles in a Marine Bacterium. mSystems 7:e0058522.
131. Woodall B, Fozo EM, Campagna SR. 2023. Dual stable isotopes enhance lipidomic studies in bacterial model organism Enterococcus faecalis. Anal Bioanal Chem 415:3593-3605.
132. Tsugawa H, Ikeda K, Takahashi M, Satoh A, Mori Y, Uchino H, Okahashi N, Yamada Y, Tada I, Bonini P, Higashi Y, Okazaki Y, Zhou Z, Zhu Z-J, Koelmel J, Cajka T, Fiehn O, Saito K, Arita M, Arita M. 2020. A lipidome atlas in MS-DIAL 4. Nature Biotechnology 38:1159-1163.
133. Tsugawa H, Nakabayashi R, Mori T, Yamada Y, Takahashi M, Rai A, Sugiyama R, Yamamoto H, Nakaya T, Yamazaki M, Kooke R, Bac-Molenaar JA, Oztolan-Erol N, Keurentjes JJB, Arita M, Saito K. 2019. A cheminformatics approach to characterize metabolomes in stable-isotope-labeled organisms. Nature Methods 16:295-298.
134. Lai Z, Tsugawa H, Wohlgemuth G, Mehta S, Mueller M, Zheng Y, Ogiwara A, Meissen J, Showalter M, Takeuchi K, Kind T, Beal P, Arita M, Fiehn O. 2018. Identifying metabolites by integrating metabolome databases with mass spectrometry cheminformatics. Nature Methods 15:53-56.
135. Tsugawa H, Cajka T, Kind T, Ma Y, Higgins B, Ikeda K, Kanazawa M, VanderGheynst J, Fiehn O, Arita M. 2015. MS-DIAL: data-independent MS/MS deconvolution for comprehensive metabolome analysis. Nat Methods 12:523-6.
136. Friedman JH, Hastie T, Tibshirani R. 2010. Regularization paths for generalized linear models via coordinate descent. Journal of Statistical Software 33:1 - 22.
137. Tay JK, Narasimhan B, Hastie T. 2023. Elastic net regularization paths for all generalized linear models. Journal of Statistical Software 106:1 - 31.
138. Mason Allison R, Johnson JG, Krampen J, Nguyen Jennifer NT, Balunas Marcy J, Schloss Patrick D. 2025. mpactR: An R adaptation of the metabolomics peak analysis computational tool (MPACT) for use in reproducible data analysis pipelines. Microbiology Resource Announcements 14:e00997-24.
139. Wang M, Carver JJ, Phelan VV, Sanchez LM, Garg N, Peng Y, Nguyen DD, Watrous J, Kapono CA, Luzzatto-Knaan T, Porto C, Bouslimani A, Melnik AV, Meehan MJ, Liu W-T, Crüsemann M, Boudreau PD, Esquenazi E, Sandoval-Calderón M, Kersten RD, Pace LA, Quinn RA, Duncan KR, Hsu C-C, Floros DJ, Gavilan RG, Kleigrewe K, Northen T, Dutton RJ, Parrot D, Carlson EE, Aigle B, Michelsen CF, Jelsbak L, Sohlenkamp C, Pevzner P, Edlund A, McLean J, Piel J, Murphy BT, Gerwick L, Liaw C-C, Yang Y-L, Humpf H-U, Maansson M, Keyzers RA, Sims AC, Johnson AR, Sidebottom AM, Sedio BE, et al. 2016. Sharing and community curation of mass spectrometry data with Global Natural Products Social Molecular Networking. Nature Biotechnology 34:828-837.
140. Shannon P, Markiel A, Ozier O, Baliga NS, Wang JT, Ramage D, Amin N, Schwikowski B, Ideker T. 2003. Cytoscape: A software environment for integrated models of biomolecular interaction networks. Genome Res 13:2498-504.
141. Pang Z, Lu Y, Zhou G, Hui F, Xu L, Viau C, Spigelman Aliya F, MacDonald Patrick E, Wishart David S, Li S, Xia J. 2024. MetaboAnalyst 6.0: Towards a unified platform for metabolomics data processing, analysis and interpretation. Nucleic Acids Research 52:W398-W406.
142. Team RDC. 2013. R: A language and environment for statistical computing, R Foundation for Statistical Computing, http://www.R-project.org/.

143. Wickham H. 2016. ggplot2: Elegant graphics for data analysis, Springer-Verlag, New York. https://ggplot2.tidyverse.org.
144. Wong B. 2011. Points of view: Color blindness. Nature Methods 8:441-441.
145. Ou J. 2021. colorBlindness: Safe color set for color blindness, https://CRAN.R-project.org/package=colorBlindnes.
146. Neuwirth E. 2022. RColorBrewer: ColorBrewer palettes, https://CRAN.R-project.org/package=RColorBrewer.
147. Vu VQ, Friendly M. 2024. ggbiplot: A grammar of graphics implementation of biplots, https://CRAN.R-project.org/package=ggbiplot.
148. Pedersen TL. 2024. ggforce: Accelerating 'ggplot2', https://CRAN.R-project.org/package=ggforce.
149. Gu Z, Gu L, Eils R, Schlesner M, Brors B. 2014. circlize implements and enhances circular visualization in R. Bioinformatics 30:2811-2.
150. Gu Z, Eils R, Schlesner M. 2016. Complex heatmaps reveal patterns and correlations in multidimensional genomic data. Bioinformatics 32:2847-9.
151. Neitmann T. 2020. mdthemes: Markdown themes for 'ggplot2', https://CRAN.R-project.org/package=mdthemes.
152. C W, B W. 2022. ggtext: Improved text rendering support for 'ggplot2', https://CRAN.R-project.org/package=ggtext.
153. Wickham H, Bryan J. 2023. readxl: Read excel files, https://CRAN.R-project.org/package=readxl.
154. Wickham H, Vaughan D, Girlich M. 2024. tidyr: Tidy messy data, https://CRAN.R-project.org/package=tidyr.
155. Bengtsson H. 2024. matrixStats: Functions that apply to rows and columns of matrices (and to vectors), https://CRAN.R-project.org/package=matrixStats.
156. Barrett T, Dowle M, Srinivasan A, Gorecki J, Chirico M, Hocking T. 2024. data.table: Extension of `data.frame`, https://CRAN.R-project.org/package=data.table.
157. Bache SM, Wickham H. 2022. magrittr: A forward-pipe operator for R, https://cran.r-project.org/web/packages/magrittr/vignettes/magrittr.html.
158. Wickham H, Pedersen TL, Seidel D. 2023. scales: Scale functions for visualization, https://CRAN.R-project.org/package=scales.
159. Wang L-G, Lam TT-Y, Xu S, Dai Z, Zhou L, Feng T, Guo P, Dunn CW, Jones BR, Bradley T, Zhu H, Guan Y, Jiang Y, Yu G. 2019. Treeio: An R package for phylogenetic tree input and output with richly annotated and associated data. Molecular Biology and Evolution 37:599-603.
160. Yu G, Smith DK, Zhu H, Guan Y, Lam TT-Y. 2017. ggtree: An R package for visualization and annotation of phylogenetic trees with their covariates and other associated data. Methods in Ecology and Evolution 8:28-36.
161. Xu S, Li L, Luo X, Chen M, Tang W, Zhan L, Dai Z, Lam TT, Guan Y, Yu G. 2022. Ggtree: A serialized data object for visualization of a phylogenetic tree and annotation data. iMeta 1:e56.
162. Bates D, Mächler M, Bolker B, Walker S. 2015. Fitting linear mixed-effects models using lme4. J of Statistical Software 67:1-48.
163. Kuznetsova A, Brockhoff PB, Christensen RHB. 2017. lmerTest package: Tests in linear mixed effects models. J of Statistical Software 82:1-26.
164. A K. 2023. ggpubr: 'ggplot2' based publication ready plots, https://CRAN.R-project.org/package=ggpubr.

1124 165. Yurekten O, Payne T, Tejera N, Amaladoss FX, Martin C, Williams M, O'Donovan C.
1125 2023. MetaboLights: open data repository for metabolomics. Nucleic Acids Research
1126 52:D640-D646.
1127 166. Vingadassalom D, Kolb A, Mayer C, Rybkine T, Collatz E, Podglajen I. 2005. An unusual
1128 primary sigma factor in the Bacteroidetes phylum. Mol Microbiol 56:888-902.
1129 167. Loferer-Krössbacher M, Klima J, Psenner R. 1998. Determination of bacterial cell dry
1130 mass by transmission electron microscopy and densitometric image analysis. Appl
1131 Environ Microbiol 64:688-94.
1132 168. Epanechnikov VA. 1969. Non-parametric estimation of a multivariate probability density.
1133 Theory of Probability & Its Applications 14:153-158.
1134 169. Poynton EF, van Santen JA, Pin M, Contreras MM, McMann E, Parra J, Showalter B,
1135 Zaroubi L, Duncan Katherine R, Linington RG. 2024. The Natural Products Atlas 3.0:
1136 Extending the database of microbially derived natural products. Nucleic Acids Research
1137 53:D691-D699.
1138 170. Wang F, Allen D, Tian S, Oler E, Gautam V, Greiner R, Metz Thomas O, Wishart
1139 David S. 2022. CFM-ID 4.0 – a web server for accurate MS-based metabolite
1140 identification. Nucleic Acids Research 50:W165-W174.
1141 171. Conroy MJ, Andrews RM, Andrews S, Cockayne L, Dennis Edward A, Fahy E, Gaud C,
1142 Griffiths William J, Jukes G, Kolchin M, Mendivelso K, Lopez-Clavijo Andrea F, Ready C,
1143 Subramaniam S, O'Donnell Valerie B. 2023. LIPID MAPS: update to databases and
1144 tools for the lipidomics community. Nucleic Acids Research 52:D1677-D1682.

1145

1146

1147 **FIGURES AND TABLES**

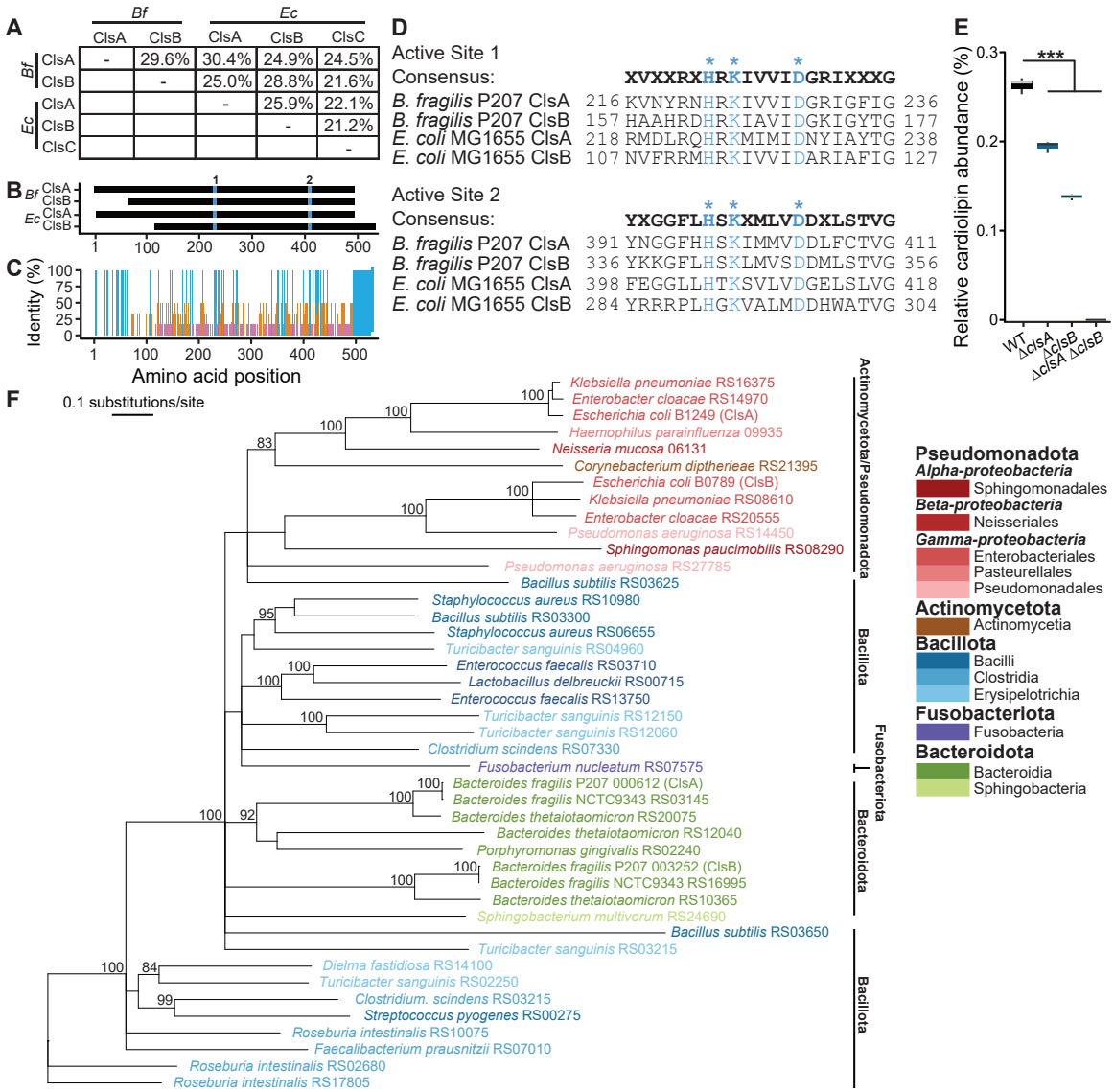

1148

1149 **Figure 1. Cardiolipin synthases diverge across the dominant gut bacterial phyla. A.** Percentage
1150 identity from pairwise amino acid alignment of cardiolipin synthases in *B. fragilis* P207 (*Bf*) and *E. coli* K12
1151 MG1655 (*Ec*). **B.** Alignment of ClsA and ClsB from *B. fragilis* P207 and *E. coli* MG1655, with the two HKD
1152 domains marked in blue. **C.** Percentage identity from amino acid alignment in panel B colored based on the
1153 thresholds <30% (pink), <100% (orange) and 100% (blue). **D.** Consensus and individual sequences of the
1154 regions flanking the two HKD active sites of *B. fragilis* and *E. coli* Cls proteins. HKD residues are colored
1155 in blue; the N- and C-terminal positions are shown. **E.** Relative abundance of cardiolipin in *B. fragilis* P207

1156 wild-type (WT), Δ*clsA*, Δ*clsB* and Δ*clsA* Δ*clsB* strains measured by mass spectrometry. The horizontal line
1157 indicates the median, and the whiskers 1.5× the interquartile range outside the 25th and 75th percentiles of
1158 n = 3 samples. (linear regression; unadjusted p-values are shown; *** indicates $p < 0.001$). **F.** Neighbor-
1159 joining tree of a Cls alignment from representative taxa of major bacterial phyla in the gut, using only one
1160 genome per species. For each sequence in the tree, taxa names are followed by genome IDs at the tip of
1161 each branch; genome accession numbers and other metadata are provided in Table S3. Bootstrap values
1162 are shown only if >80%. Bacterial taxa are colored according to the phylum to which they belong (red,
1163 Pseudomonadota – 3 classes with 1, 1, and 3 families; brown, Actinomycetota – 1 class; blue, Bacillota –
1164 3 classes; violet, Fusobacteriota – 1 class; green, Bacteroidota – 2 classes, respectively). Key indicates the
1165 rate of amino acid substitutions per site.
1166
1167

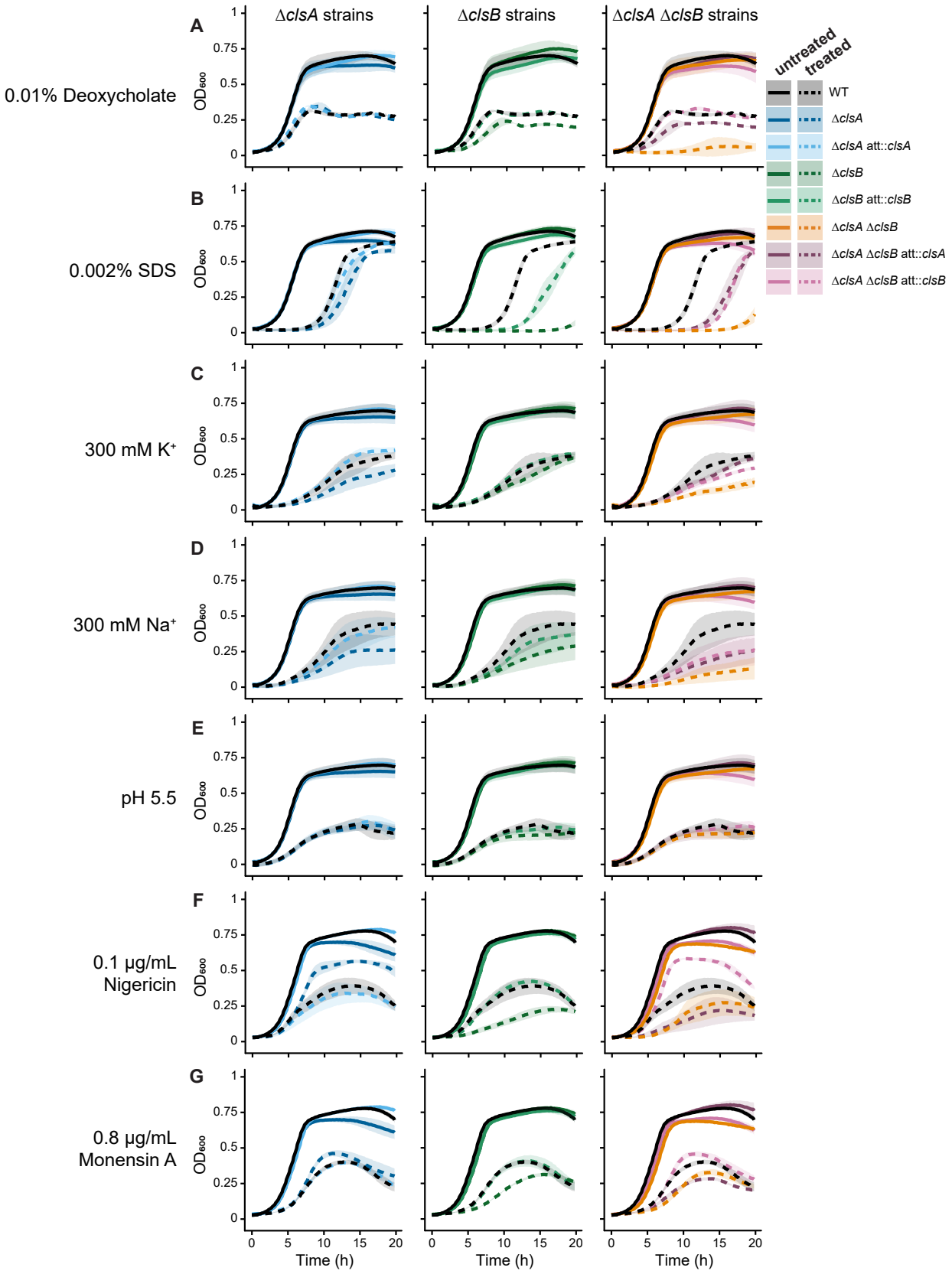
ΔclsA strains
ΔclsB strains
ΔclsA ΔclsB strains
A
B
C
D
E
F
G
0.01% Deoxycholate
0.002% SDS
300 mM K+
300 mM Na+
pH 5.5
0.1 µg/mL Nigericin
0.8 µg/mL Monensin A
OD600
Time (h)
untreated
treated
WT
ΔclsA
ΔclsA att::clsA
ΔclsB
ΔclsB att::clsB
ΔclsA ΔclsB
ΔclsA ΔclsB att::clsA
ΔclsA ΔclsB att::clsB

1168

1169 **Figure 2. Loss of cardiolipin synthase activity results in growth defects under stress.** Optical density
1170 (OD_{600}) measurements of *B. fragilis* P207 wild-type (WT) and *cls* single or double mutant strains exposed
1171 to the detergents (**A.**) 0.01% deoxycholate or (**B.**) 0.002% SDS; the salts (**C.**) 300 mM K^+ or (**D.**) 300 mM
1172 Na^+; (**E.**) medium adjusted to pH 5.5; and the ionophores (**F.**) 0.1 µg/mL nigericin or (**G.**) 0.8 µg/mL
1173 monensin A. Untreated (solid lines) and treated cultures (dashed lines) are plotted by strain, with blue,
1174 green and orange/purple indicating *clsA*-, *clsB*- and *clsA clsB*-related strains, respectively. Black indicates
1175 WT. The shaded areas around each line indicate 2× the standard error of the mean of n = 3 biological
1176 replicates.
1177

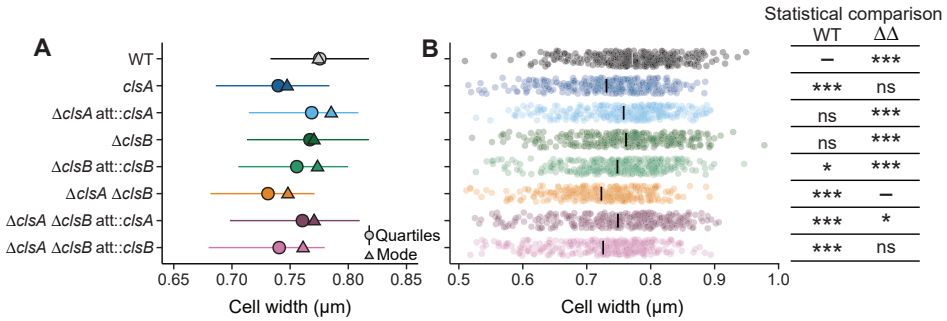

Figure 3. Loss of cardiolipin synthase activity is associated with defects in cell width. A. Summary of the cell width distributions. Horizontal line lengths indicate the 25% and 75% quartiles of the distribution; circles indicate the median; triangles indicates the mode (i.e., the peak of the distribution). **B.** Cell width data for all cells shown in A. plotted by strain (n = 323 cells/strain). The gray or black bars indicate the mean. The table at right shows the results of a mixed-effect linear model comparing strain width to the widths of either WT cells or Δ*clsA* Δ*clsB* double mutant (ΔΔ) cells, as indicated at the top of the column, with a random intercept of biological replicate (i.e., cell width ~ strain + 1|biological replicate). Unadjusted p-values are shown; *, $p < 0.05$, *** $p < 0.001$.

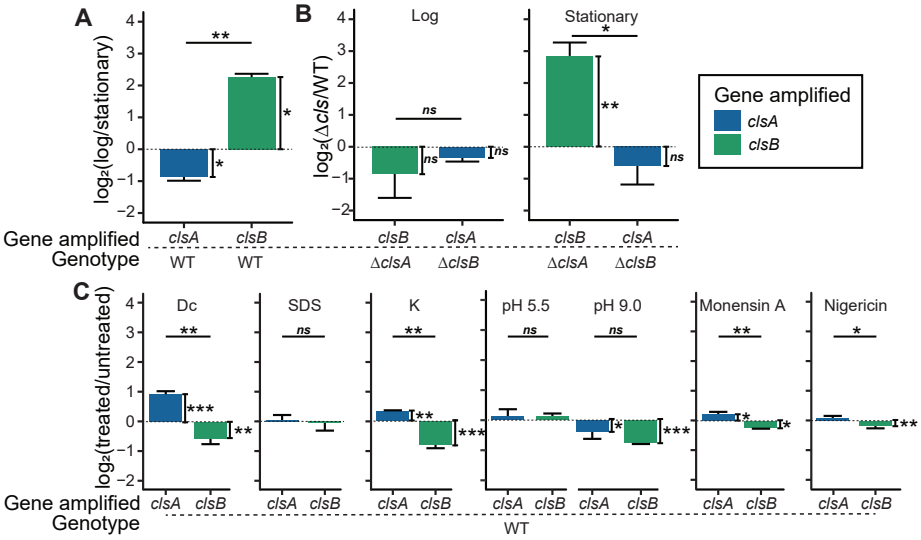

Figure 4. Cardiolipin synthase genes have distinct expression patterns. A. RT-qPCR analysis of relative levels of *clsA* and *clsB* transcripts, shown as the $\log_2$ ratios between log- and stationary-phase growth. **B.** Expression levels of *clsA* or *clsB* when the other gene is knocked out in log- or stationary-phase growth. **C.** *clsA* and *clsB* expression levels in WT *B. fragilis* P207 after 20 min exposure to of 0.01% deoxycholate, 0.002% SDS, 300 mM K, pH 5.5, pH 9.0, 0.8 µg/mL monensin A, or 0.1 µg/mL nigericin. For all panels, values are means ± standard deviation from three biological replicates, each biological replicate value being the mean of three technical replicates. The vertical brackets for statistical analysis assess the significance of the difference between conditions in A and C, between mutant and WT in B. The horizontal brackets for statistical analysis assess the significance of the difference between ΔΔCt values for *clsA* and *clsB* (Students *t*-test). Genes amplified are colored in blue (*clsA*) or green (*clsB*). Error bars indicate standard deviation. Unadjusted p-values are shown; *, $p < 0.05$; **, $p < 0.01$; ***, $p < 0.001$.

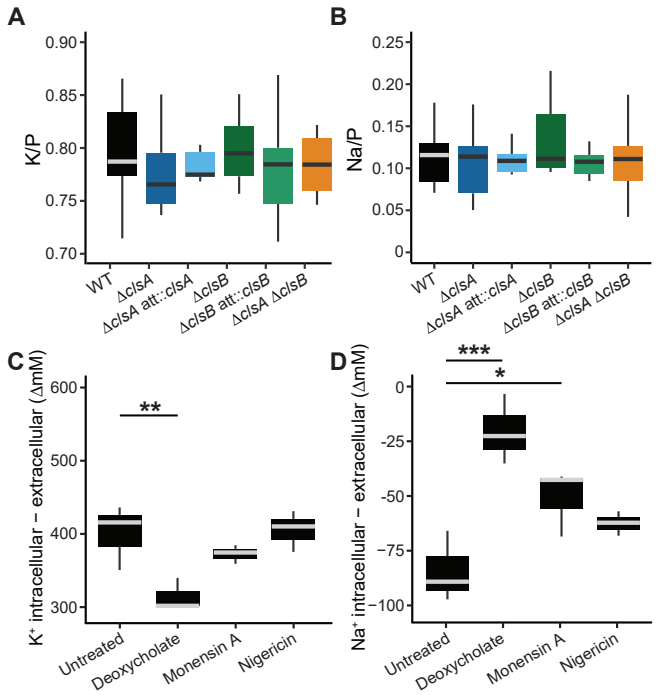

Figure 5. Stress but not loss of Cls function disrupts membrane ion gradients. A., B. Abundance of (**A.**) potassium (K) and (**B.**) sodium (Na) normalized to intracellular phosphorus (P) in *B. fragilis* P207 WT, Δ*clsA*, Δ*clsB* and complemented strains as well as the Δ*clsA* Δ*clsB* strain, as detected by inductively coupled plasma mass spectrometry (ICP-MS). **C., D.** Differential concentrations of (**C.**) K^+ and (**D.**) Na^+ in WT strain cells after a 20 min exposure to 0.01% deoxycholate, 0.8 µg/mL monensin A or 0.1 µg/mL nigericin (linear regression). The intracellular concentrations (i.e., normalized to cell volume and number of colony-forming units) with the extracellular concentrations subtracted are shown. For all boxplots, gray or black lines indicate the median; the top and bottom edges of the box indicate the 25th and 75th percentiles of the data; the error bars indicate standard deviation (10 biological replicates for untreated conditions and three for the treatment conditions). Unadjusted p-values are shown; *, $p < 0.05$; **, $p < 0.01$; ***, $p < 0.001$.

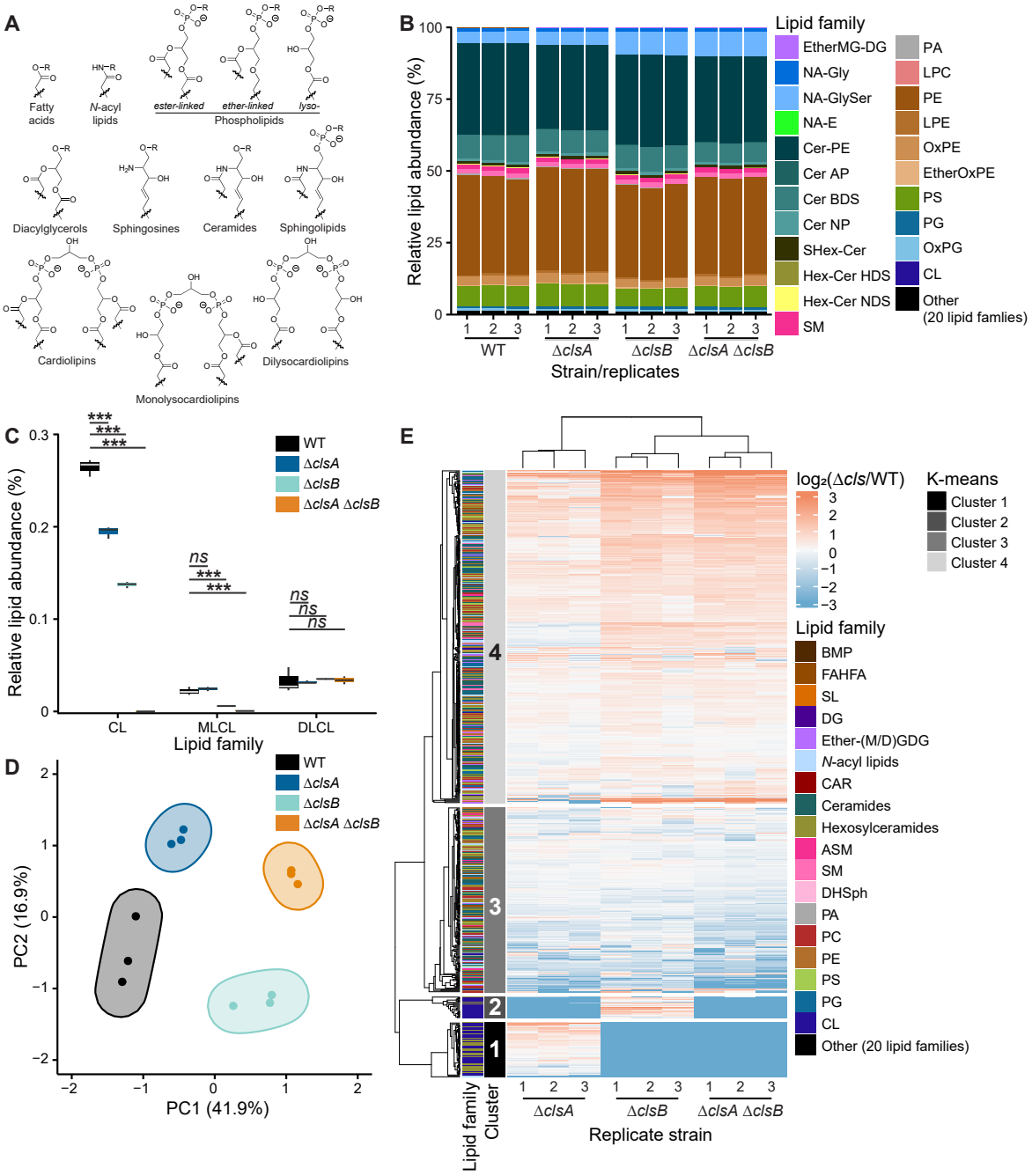

Figure 6. Paralogous cardiolipin synthases produce unique lipid products. A. Structures of lipid families detected by UHPLC-MS/HRMS. For fatty acids, the R-group is H; for saccharolipids, a sugar (i.e., lipid A); and for acyl carnitines, a carnitine. The R-group is H for phosphatidic acid and ethanolamine for phosphatidylethanolamine. Phospholipids are shown as members of three categories: ester-linked (i.e., classical phospholipids), ether-linked and lysophospholipids. Diacylglycerols and monogalactosyl /

1221 monoglucosyl-diacyglycerols have H or a hexose ring as an R-group, respectively. Ceramides, which can
1222 be conjugated to a hexose (i.e., hexosylceramide), are synthesized by *N*-acylating a sphingosine. As
1223 phosphorylated ceramides, sphingolipids have similar R-groups as phospholipids. Length and unsaturation
1224 of the acyl tails are not shown. **B.** Relative abundance of lipid species across WT, Δ*clsA,* Δ*clsB and* Δ*clsA*
1225 Δ*clsB* strains (three biological replicates). Lipid families are abbreviated as follows: PC indicates
1226 phosphatidylcholine; PA, phosphatidic acid; PE, phosphatidylethanolamine; PG, phosphatidylglycerol; PS,
1227 phosphatidylserine; CL, cardiolipin. L-, ML- and DL- indicate lyso-, monolyso- and dilyso-, respectively. **C.**
1228 Relative abundance of cardiolipin, monolyso-cardiolipin and dilysocardiolipin (linear regression).
1229 Unadjusted p-values are shown; ***, $p < 0.001$. **D.** Principal component analysis plot of lipid species in each
1230 strain, with the minimum volume–enclosing ellipses estimated by the Khachiyan algorithm. **E.** Heatmap
1231 representation of the $\log_2$(fold change) of lipid species in each knockout strain compared to WT. Columns
1232 are clustered by similarity and rows by K-means. The left side of the heatmap shows lipid families and K-
1233 means clusters.
1234

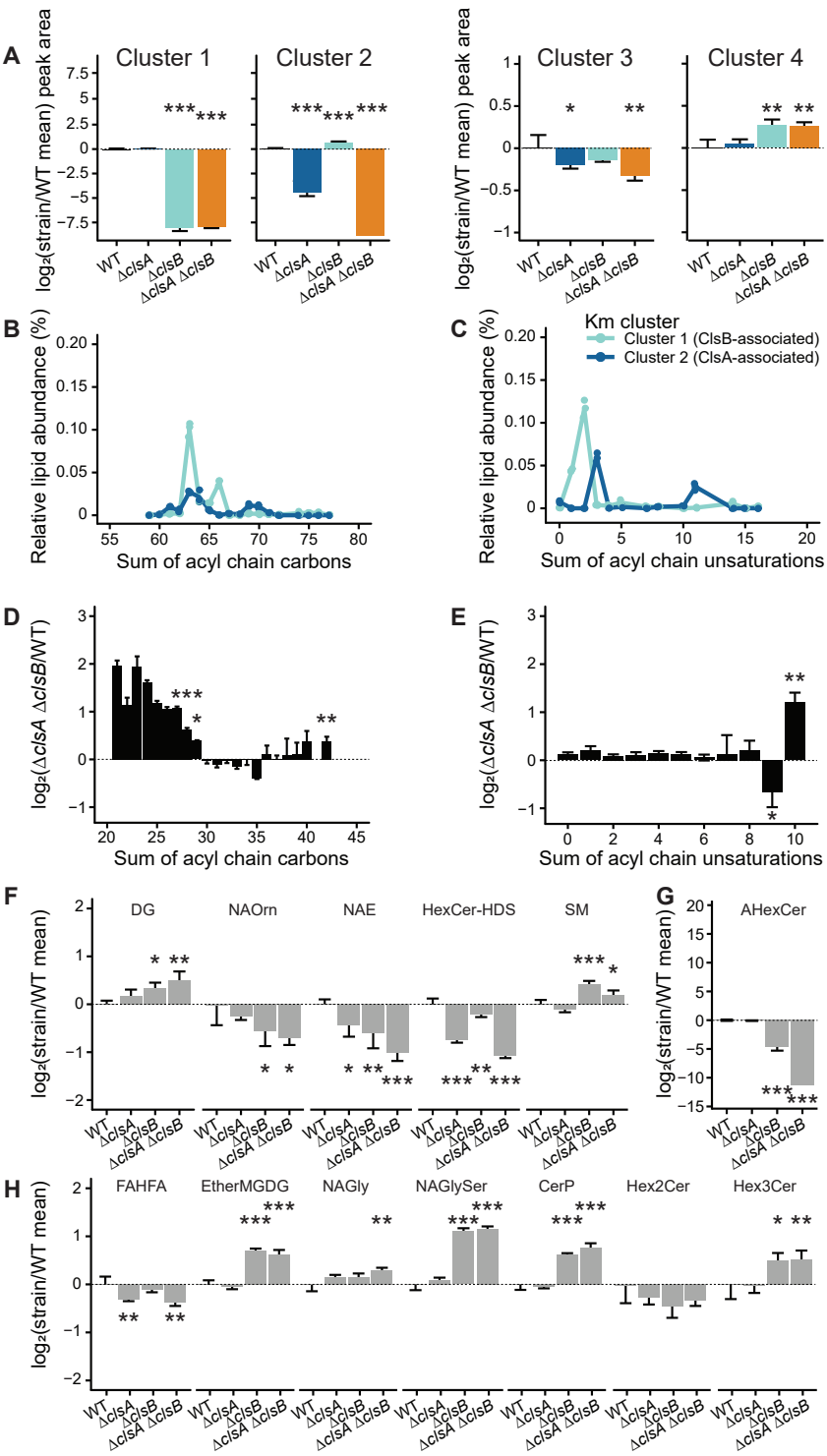

Figure 7. Cardiolipin synthases shape the length and unsaturation level of membrane lipid acyl chains. A. $\log_2$(fold change) of the total peak areas for all lipids in k-means clusters compared to the mean of WT peak areas of that particular cluster (linear regression of peak areas compared to WT). **B., C.** Relative

1239 distribution of sum of acyl chain (**B.**) carbons and (**C.**) unsaturations in cardiolipin and monolysocardiolipin
1240 species of Km clusters 1 (ClsB-associated) and 3 (ClsA-associated) in WT cells. **D., E.** $\log_2$(fold change) of
1241 total two acyl-tailed phospholipids in Δ*clsA* Δ*clsB* strain cells compared to WT shown by (**D.**) acyl chain
1242 length and (**E.**) unsaturations. Student's *t*-test comparing values at designated x-axis values); nd, not
1243 detected (i.e., 0) in the Δ*clsA* Δ*clsB* strain. **F., G., H.** $\log_2$(fold change) of lipids detected in negative (**F.**) and
1244 positive (**G., H.**) ionization mode UHPLC-MS/HRMS comparing each strain to the mean WT peak area.
1245 AHexCer was detected in only 2 and 1 replicates of Δ*clsB* and Δ*clsA* Δ*clsB*, respectively. Lipid families are
1246 abbreviated as follows: DG, diacylglycerol; MG, monogalactosyl/monoglucosyl conjugation; NA, *N*-acyl,
1247 with substituent conjugations indicated for glycyl- (Gly), glycylseryl- (GlySer, ornithine- (Orn), and
1248 ethanolamine- (E); CER, ceramide, with A indicating acyl-, P indicating phospho- and Hex, Hex2 and Hex3
1249 indicating hexosyl-, dihexosyl-, and trihexosyl-; HDS, hydroxy fatty acid-dihydrosphingosine; SM,
1250 sphingomyelin; Ether-, ether-linked (linear regression compared to WT). Across all panels, error bars
1251 indicate standard deviation. Unadjusted p-values are shown; *, $p < 0.05$; **, $p < 0.01$; ***, $p < 0.001$.
1252

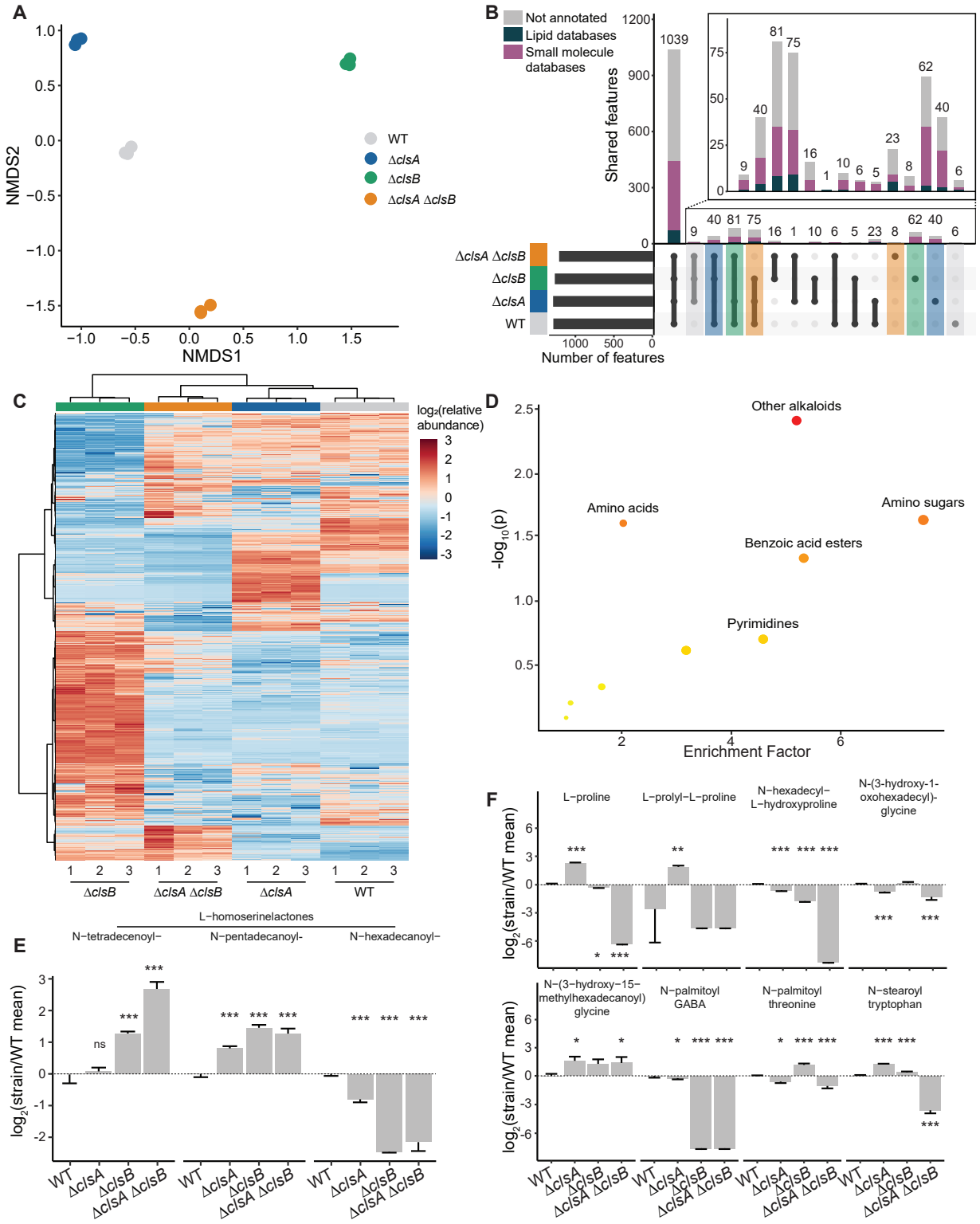

Figure 8. Cardiolipin synthases disrupt metabolic homeostasis. A. NMDS of metabolomics data colored by strain. **B.** Upset plot with the main bar plot color coded for the metabolomic features annotation

1256 sources (dark green = lipid databases, purple = small molecule databases, grey = not annotated within
1257 5ppm error) and the lower section color coded for metabolomic features only present or absent in each
1258 strain (grey = WT, blue = Δ*clsA,* green = Δ*clsB*, orange = Δ*clsA* Δ*clsB*). Inset is a rescaled axis of
1259 metabolites missing in at least one strain. **C.** Heatmap of row normalized abundance of each metabolite in
1260 each strain, clustering by metabolomic features on the vertical axis and samples on the horizontal axis
1261 using Euclidean distance and Ward clustering (3 technical replicates shown for each strain). **D.** Metabolic
1262 pathway analysis with nonlipid sub-categories of *clsAclsB* knockout compared to wildtype (≥3
1263 features/pathway). The x-axis represents the enrichment factor computed from pathway topological
1264 analysis on non-lipid species, and the y-axis is the log of p-value obtained from pathway enrichment
1265 analysis. The pathways that were most significantly changed are characterized by both a high-log(p) value
1266 and high enrichment factor (top right region). **E., F.** Abundance of compounds in enriched pathways for (E)
1267 lipid-conjugated homoserine lactones and (F) fatty amides (top enriched pathways) (mean and standard
1268 deviation of 3 technical replicates shown; linear regression compared to WT). Across all panels, error bars
1269 indicate standard deviation. Unadjusted p-values are shown; *, $p < 0.05$; **, $p < 0.01$; ***, $p < 0.001$.
1270

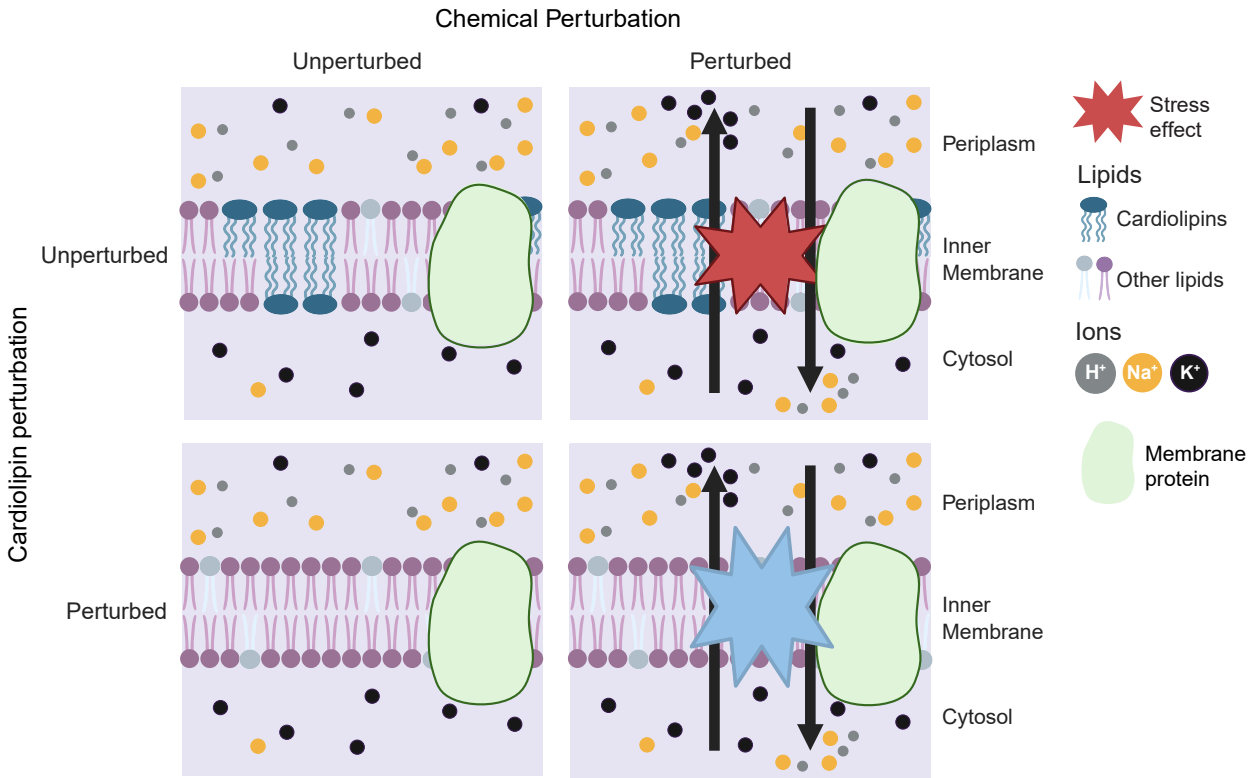

Figure 9. Cardiolipins support fitness under membrane perturbing conditions. In unperturbed cells, ion gradients are maintained across the inner membrane, with higher extracellular concentrations of H^+ and Na^+ and elevated intracellular K^+ (top left). The outer membrane is generally permeable to these ions due to the presence of porins. In the absence of cardiolipin, *B. fragilis* remodels its membrane lipid composition, which presumably helps to maintain ion gradients (bottom left). Chemical membrane (or membrane ion gradient) perturbation alters *cls* gene expression and ion homeostasis (top right). In the absence of cardiolipins, cells are more susceptible to chemical membrane perturbations (bottom right). The larger blue star indicates the greater fitness cost associated with membrane perturbation in cardiolipin-deficient cells, particularly *clsB* mutants. In contrast, the smaller red star reflects reduced stress susceptibility in cells that retain cardiolipin synthesis.

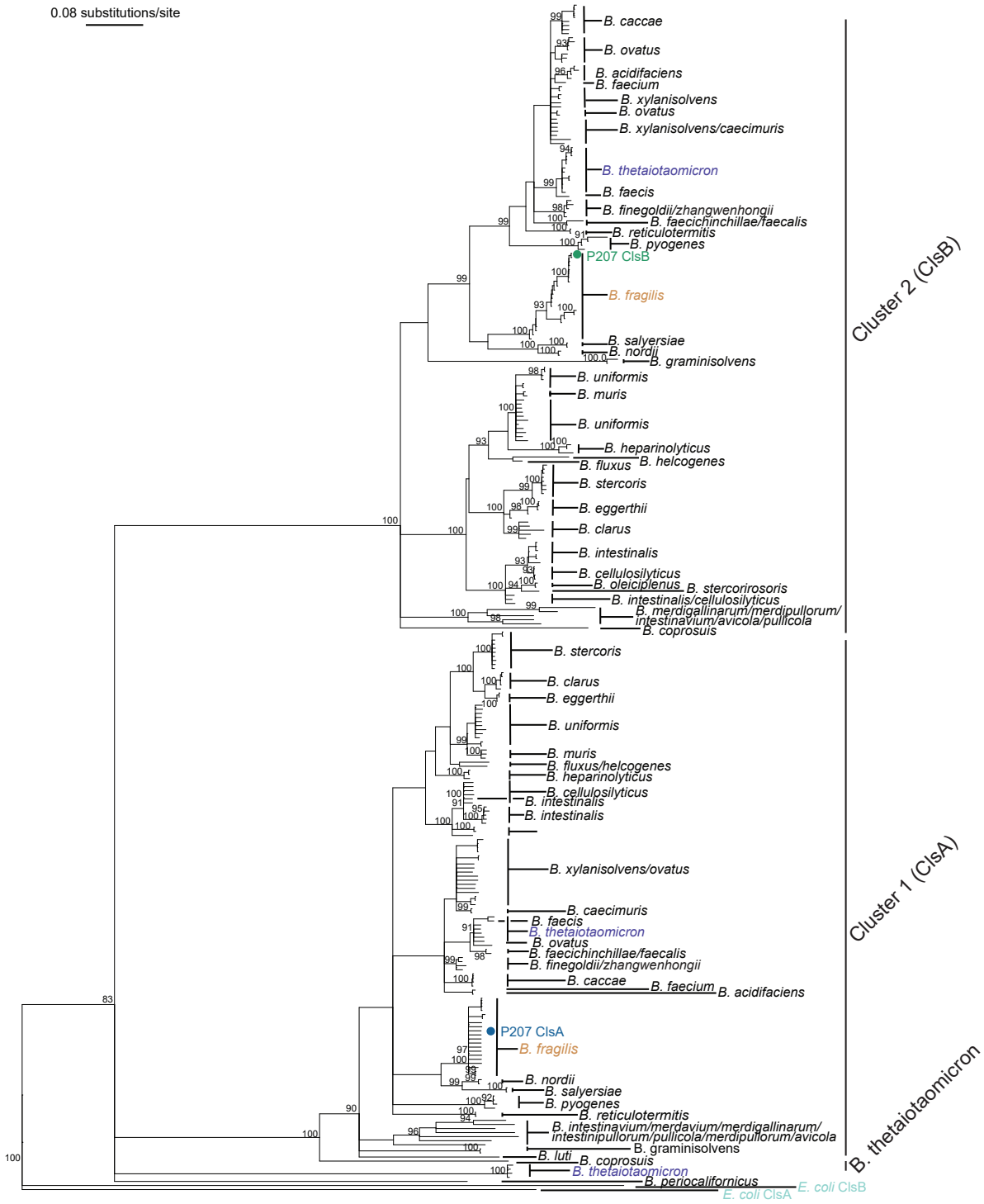

Figure S1. Neighbor-joining tree of cardiolipin synthases from *Bacteroides* species. Clusters 1 (ClsA), 2 (ClsB) and 3 (not named) of *Bacteroides* Cls proteins are indicated. *E. coli* ClsA was designated as an outgroup. ClsA and ClsB of *B. fragilis* P207 are colored in blue and green, respectively. Other strains

1286 of *B. fragilis, B. thetaiotaomicron*, and *E. coli* are colored in gold, purple and light blue, respectively. Taxa
1287 labels with similar tree positions are combined for clarity at times (i.e., *B. xylanisolvens/caecimuris*). Key
1288 indicates the rate of amino acid substitutions per site. Bootstrap values are generally shown only if ≥90.
1289

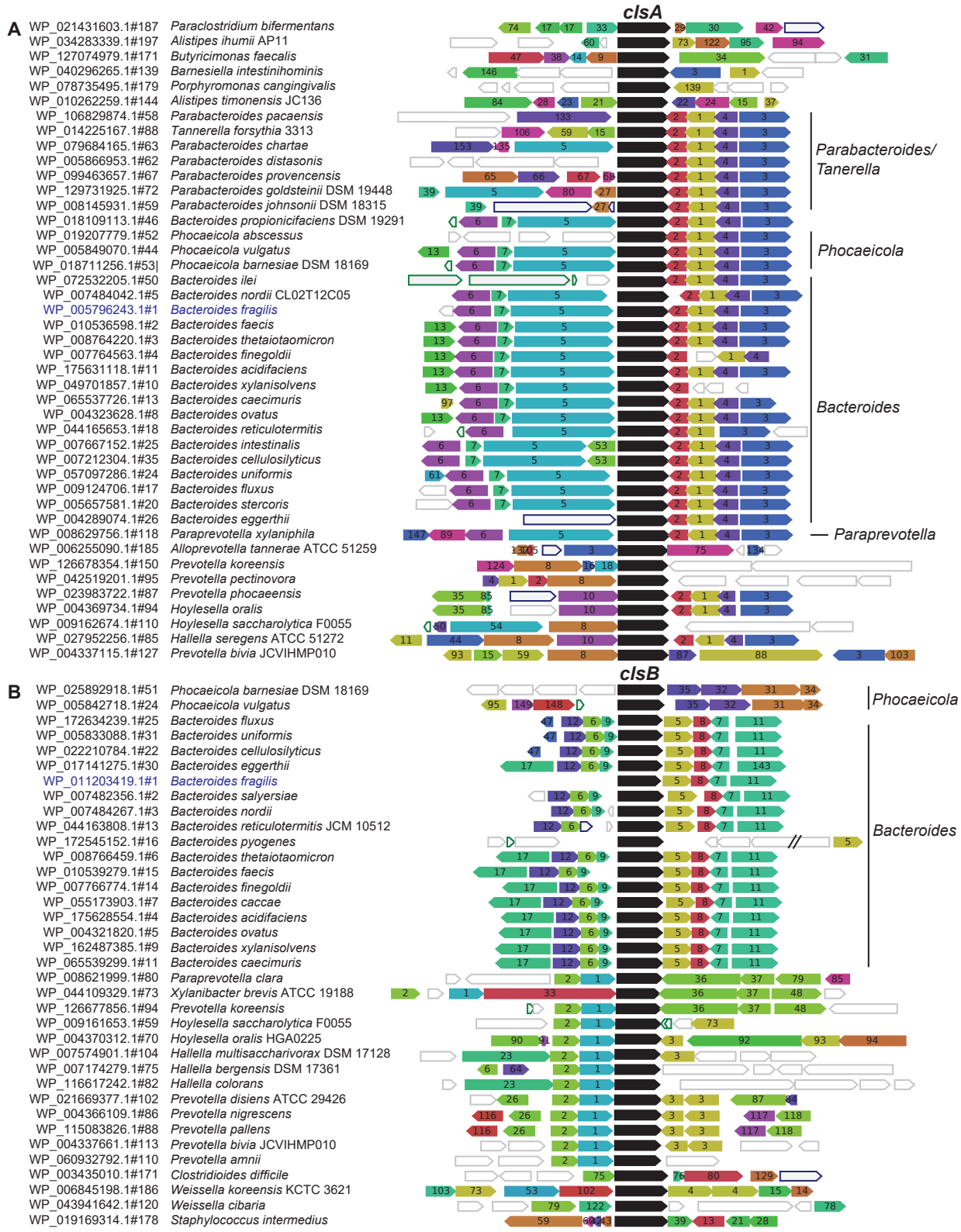
A
clsA
WP_021431603.1#187 Paraclostridium bifermentans
WP_034283339.1#197 Alistipes ihumii AP11
WP_127074979.1#171 Butyricimonas faecalis
WP_040296265.1#139 Barnesiella intestinihominis
WP_078735495.1#179 Porphyromonas cangingivalis
WP_010262259.1#144 Alistipes timonensis JC136
WP_106829874.1#58 Parabacteroides pacaensis
WP_014225167.1#88 Tannerella forsythia 3313
WP_079684165.1#63 Parabacteroides chartae
WP_005866953.1#62 Parabacteroides distasonis
WP_099463657.1#67 Parabacteroides provencensis
WP_129731925.1#72 Parabacteroides goldsteinii DSM 19448
WP_008145931.1#59 Parabacteroides johnsonii DSM 18315
WP_018109113.1#46 Bacteroides propionicifaciens DSM 19291
WP_019207779.1#52 Phocaeicola abscessus
WP_005849070.1#44 Phocaeicola vulgatus
WP_018711256.1#53 Phocaeicola barnesiae DSM 18169
WP_072532205.1#50 Bacteroides ilei
WP_007484042.1#5 Bacteroides nordii CL02T12C05
WP_005796243.1#1 Bacteroides fragilis
WP_010536598.1#2 Bacteroides faecis
WP_008764220.1#3 Bacteroides thetaiotaomicron
WP_007764563.1#4 Bacteroides finegoldii
WP_175631118.1#11 Bacteroides acidifaciens
WP_049701857.1#10 Bacteroides xylanisolvens
WP_065537726.1#13 Bacteroides caecimuris
WP_004323628.1#8 Bacteroides ovatus
WP_044165653.1#18 Bacteroides reticulotermitis
WP_007667152.1#25 Bacteroides intestinalis
WP_007212304.1#35 Bacteroides cellulosilyticus
WP_057097286.1#24 Bacteroides uniformis
WP_009124706.1#17 Bacteroides fluxus
WP_005657581.1#20 Bacteroides stercoris
WP_004289074.1#26 Bacteroides eggerthii
WP_008629756.1#118 Paraprevotella xylaniphila
WP_006255090.1#185 Alloprevotella tannerae ATCC 51259
WP_126678354.1#150 Prevotella koreensis
WP_042519201.1#95 Prevotella pectinovora
WP_023983722.1#87 Prevotella phocaeensis
WP_004369734.1#94 Hoylesella oralis
WP_009162674.1#110 Hoylesella saccharolytica F0055
WP_027952256.1#85 Hallella seregens ATCC 51272
WP_004337115.1#127 Prevotella bivia JCVIHMP010
Parabacteroides/ Tanerella
Phocaeicola
Bacteroides
Paraprevotella
B
clsB
WP_025892918.1#51 Phocaeicola barnesiae DSM 18169
WP_005842718.1#24 Phocaeicola vulgatus
WP_172634239.1#25 Bacteroides fluxus
WP_005833088.1#31 Bacteroides uniformis
WP_022210784.1#22 Bacteroides cellulosilyticus
WP_017141275.1#30 Bacteroides eggerthii
WP_011203419.1#1 Bacteroides fragilis
WP_007482356.1#2 Bacteroides salyersiae
WP_007484267.1#3 Bacteroides nordii
WP_044163808.1#13 Bacteroides reticulotermitis JCM 10512
WP_172545152.1#16 Bacteroides pyogenes
WP_008766459.1#6 Bacteroides thetaiotaomicron
WP_010539279.1#15 Bacteroides faecis
WP_007766774.1#14 Bacteroides finegoldii
WP_055173903.1#7 Bacteroides caccae
WP_175628554.1#4 Bacteroides acidifaciens
WP_004321820.1#5 Bacteroides ovatus
WP_162487385.1#9 Bacteroides xylanisolvens
WP_065539299.1#11 Bacteroides caecimuris
WP_008621999.1#80 Paraprevotella clara
WP_044109329.1#73 Xylanibacter brevis ATCC 19188
WP_126677856.1#94 Prevotella koreensis
WP_009161653.1#59 Hoylesella saccharolytica F0055
WP_004370312.1#70 Hoylesella oralis HGA0225
WP_007574901.1#104 Hallella multisaccharivorax DSM 17128
WP_007174279.1#75 Hallella bergensis DSM 17361
WP_116617242.1#82 Hallella colorans
WP_021669377.1#102 Prevotella disiens ATCC 29426
WP_004366109.1#86 Prevotella nigrescens
WP_115083826.1#88 Prevotella pallens
WP_004337661.1#113 Prevotella bivia JCVIHMP010
WP_060932792.1#110 Prevotella amnii
WP_003435010.1#171 Clostridioides difficile
WP_006845198.1#186 Weissella koreensis KCTC 3621
WP_043941642.1#120 Weissella cibaria
WP_019169314.1#178 Staphylococcus intermedius
Phocaeicola
Bacteroides

1290

1291 **Figure S2. Genomic neighborhood synteny indicates the ancestral introduction of *clsA* and *clsB***
1292 **into the *Bacteroides.*** Curated WebFlags2 output of (**A.**) *clsA* and (**B.**) *clsB* genomic neighborhoods. *B.*
1293 *fragilis* is colored blue. Genera of interest with similar levels of gene conservation are indicated at right.
1294

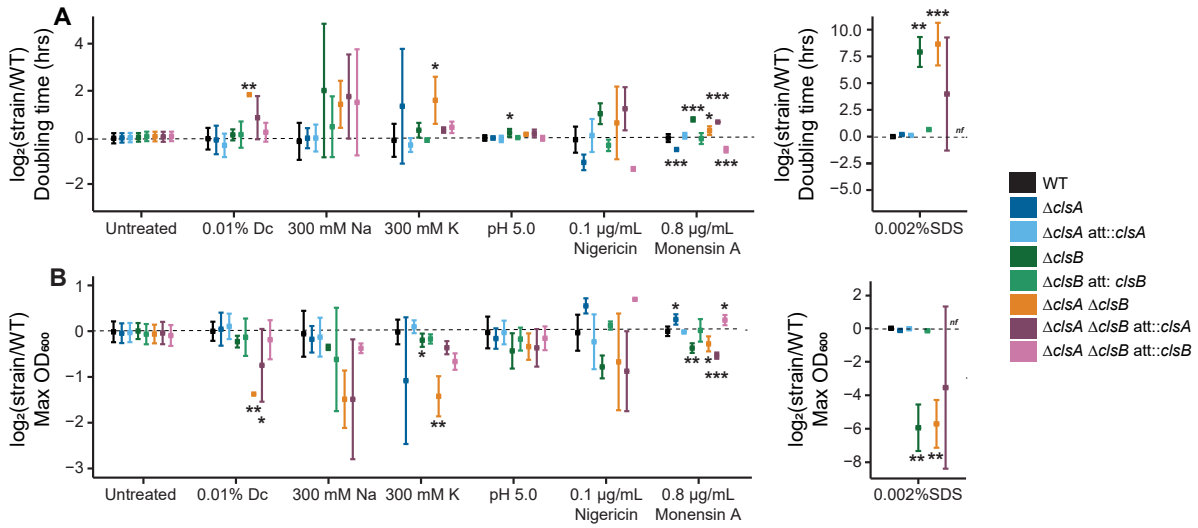

Figure S3. Loss of cardiolipin synthase activity results in growth defects under stress. A., B. $\log_2$(fold change) of (**A.**) doubling time and (**B.**) maximum OD_{600} comparing *B. fragilis* wild-type (WT) and *cls* mutants to the average of WT in that condition. Metrics were calculated from 24-h growth curves in BHIS medium alone or containing 0.01% deoxycholate (Dc), 0.002% sodium dodecyl sulfate (SDS), 300 mM sodium (Na^+), 300 mM potassium (K^+), and 0.01 µg/mL nigericin and 0.8 µg/mL monensin A. Any doubling time ≥100 h was considered as no growth. The dashed horizontal line indicates no change from the average of WT. Strain are colored with blue (*clsA-related*), green (*clsB*-related) and orange/purple (*clsA clsB*-related). Black indicates WT. The vertical lines indicate mean; the ends of the whiskers ± standard deviation (linear regression compared to WT). Three biological replicates for each condition were run, each run in technical triplicate. nf, no accurate fit of growth data by the polynomial was found. Unadjusted p-values are shown; *, $p < 0.05$; **, $p < 0.01$; ***, $p < 0.001$.

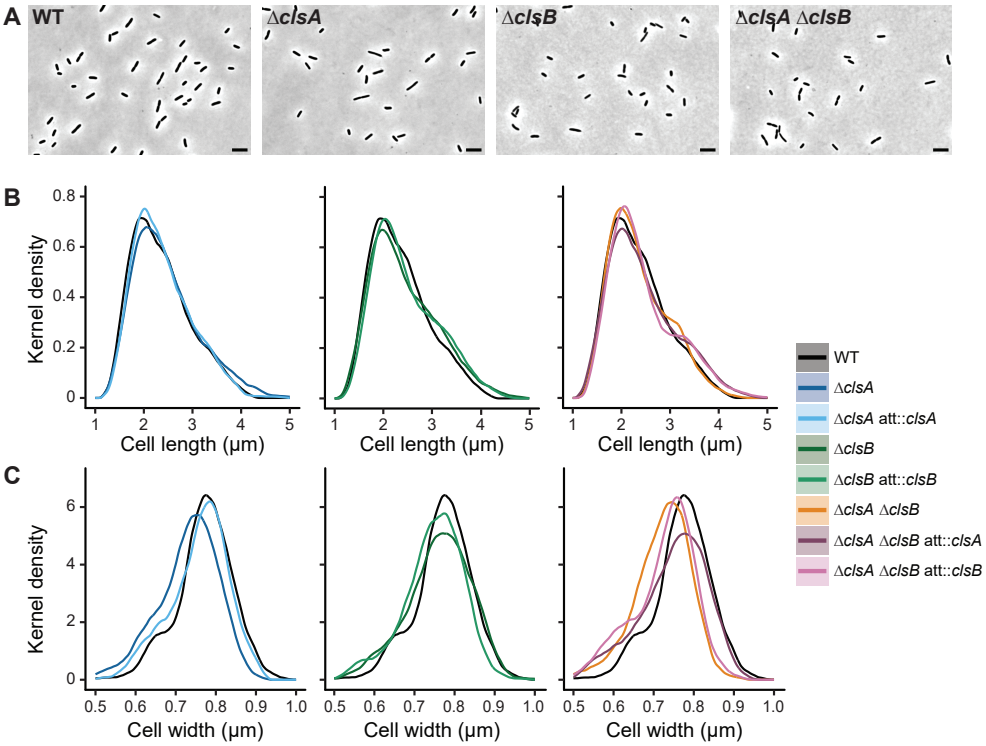

1309

1310 **Figure S4. Loss of cardiolipin synthase activity is associated with defects in cell width. A.** Phase-

1311 contrast microscopy images of *B. fragilis* P207 WT, Δ*clsA*, Δ*clsB* and Δ*clsA* Δ*clsB* strains. Scale bars, 5 μm.

1312 **B., C.** Distributions estimated by kernel density of (**B.**) cell length and (**C.**) cell width. Results are plotted by

1313 strain with blue, green and orange/purple indicating *clsA*-, *clsB*- and *clsA clsB*-related strains, respectively.

1314 Black indicates WT.

1315

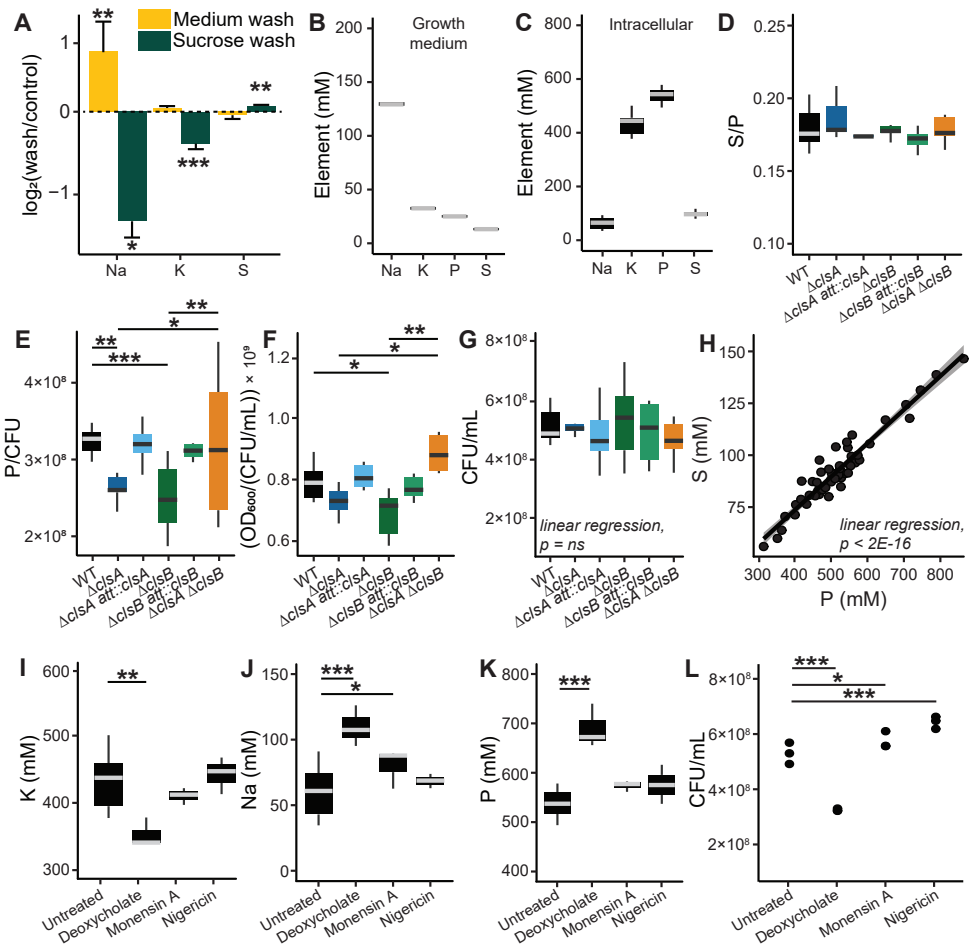

Figure S5. Washing but not loss of *cls* genes disrupts intracellular elemental concentrations. Inductively coupled plasma mass spectrometry (ICP-MS) analysis using wash-free sample preparation to quantify intracellular elemental concentrations. **A.** $\log_2$(fold change) of elements comparing unwashed cells to cell pellets washed with either BHIS growth medium or an isotonic sucrose solution. Error bars indicate standard deviation. **B.** Concentrations of detected elements in BHIS growth medium. **C.** Intracellular concentrations of detected elements in WT *B. fragilis* P207. **D.** Intracellular sulfur in *B. fragilis* P207 strains normalized to P. **E.** Intracellular phosphorus (P) per 10^6 colony-forming units (CFU) in *B. fragilis* P207 wild-type (WT), Δ*clsA*, Δ*clsB* and Δ*clsA* Δ*clsB* strains. **F.** OD_{600} normalized to CFU per mL of strain cultures used in ICP-MS input. **G.** Raw CFU/mL of each strain shown in panels F and G. **H.** Intracellular P content compared to sulfur (S) content across *cls* strains and treatment conditions. **I., J.** Intracellular concentrations of (**I.**) K^+ and (**J.**) Na^+ after a 20 min exposure to 0.01% deoxycholate, 0.8 µg/mL monensin A and 0.1 µg/mL nigericin. Each treatment had the same culture input. **K.** Intracellular P concentrations of *B. fragilis* WT cells

1329 after 20 min of exposure to the indicated stress conditions. **L.** CFU/mL of strain cultures after exposure to
1330 the treatments in **I–L**. For all boxplots, the gray or black middle lines indicate the median; the top and
1331 bottom edges of the box indicate the 25th and 75th percentiles of n = 3 replicates for wash and treatment
1332 experiments and n = 10 replicates for rest. Whiskers indicate 1.5× the interquartile range (IQR). For the
1333 linear regression, the shade ribbon indicates standard error of the mean. All statistical comparisons were
1334 made using linear regression, with unadjusted p-values shown; *, $p < 0.05$; **, $p < 0.01$; ***, $p < 0.001$.
1335

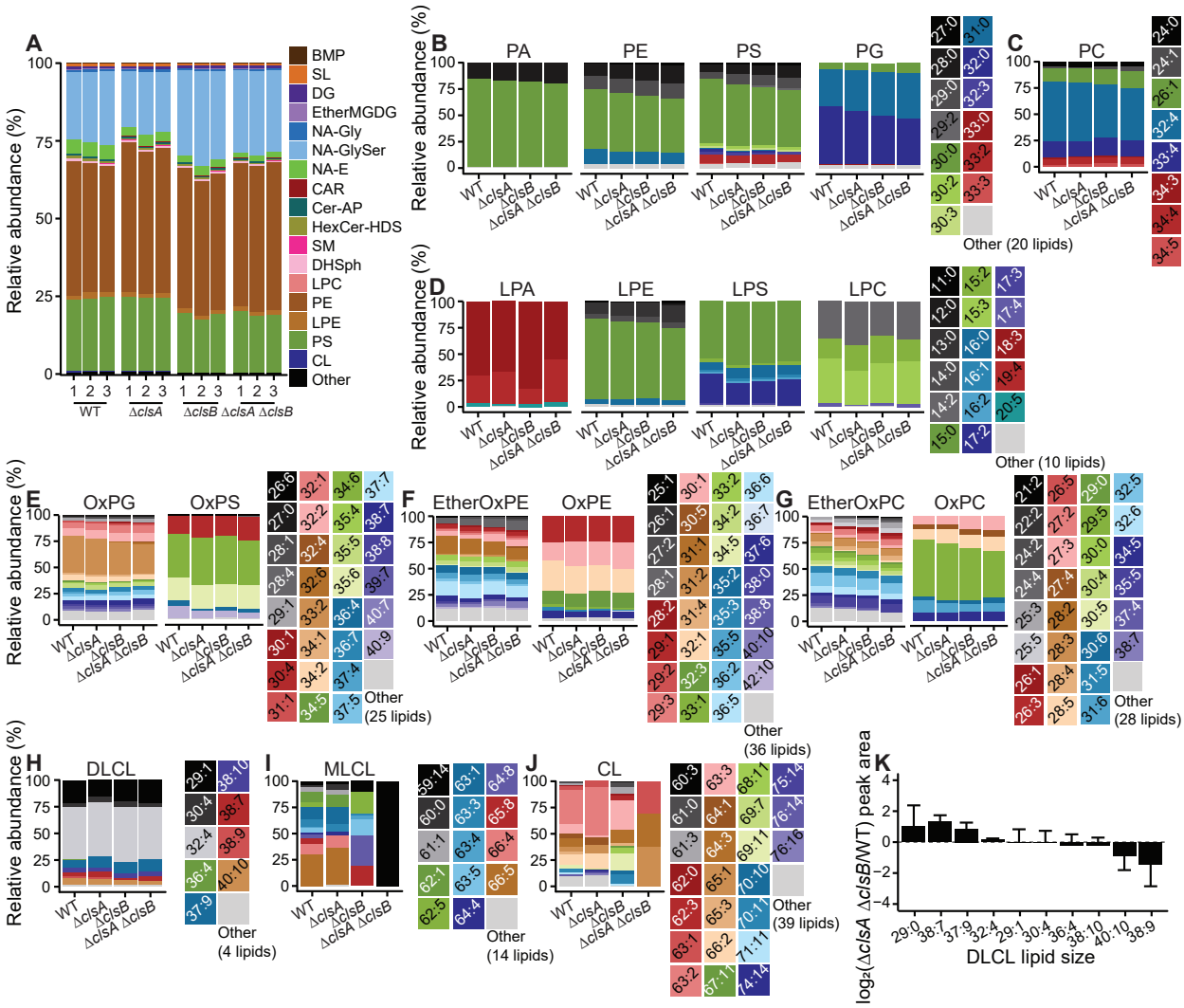

Figure S6. Cardiolipin synthases shape the membrane lipid population. A-J. Relative abundance of lipid species in membranes across *B. fragilis* WT, Δ*clsA*, Δ*clsB*, and Δ*clsA* Δ*clsB* strains in positive (**A.**) or negative (**B-J.**) electrospray ionization modes for UHPLC–MS/HRMS. For **A,** colors designate lipid family. Positive-mode lipid families are abbreviated as follows: BMP, bismonoacylglycerophosphate; SL, saccharolipids; DG, diacylglycerol; EtherMG, ether-linked with monogalactosyl/monoglucosyl conjugation; NA, *N*-acyl, with substituent conjugations indicated for glycyl- (Gly), glycylserine- (GlySer), and ethanolamine- (E); CAR, acylcarnitine; CER, ceramide, AP indicating alpha-hydroxy fatty acid-phytospingosine and Hex indicating hexosyl-; SM, sphingomyelin; DHSph, sphinganine (please see the legend for panel E for other abbreviations). For **B-J**, species are colored based on the total number of

1347 carbons in their acyl chains. Lipids at <1% abundance are colored gray, with the number of lipid species in
1348 this category indicated in the figure. Relative abundance plots are grouped as (**B.**) two or (**C.**) one acyl-
1349 tailed phospholipid species, with oxidized and ether-linked lipids shown in **E.-G.**, or (**H.**) dilysocardiolipin,
1350 (**I.**) monolysocardiolipin or (**J.**) cardiolipin species. Negative-mode lipid families are abbreviated as follows:
1351 PA, phosphatidic acid; PE, phosphatidylethanolamine; PS, phosphatidylserine; PG, phosphatidylglycerol;
1352 PC, phosphatidylcholine; CL, cardiolipin. L-, ML- and DL- indicate lyso-, monolyso- and dilyso-, respectively.
1353 Ox and Ether indicate oxidized and ether-linked, respectively. **K.** $\log_2$(fold change) peak area of
1354 dilysocardiolipin species comparing Δ*clsA* Δ*clsB* to WT (linear regression, $p < 0.00029$; $\log_{10}$[peak area] ~
1355 strain + DLCL species). Error bars indicate standard deviation.
1356

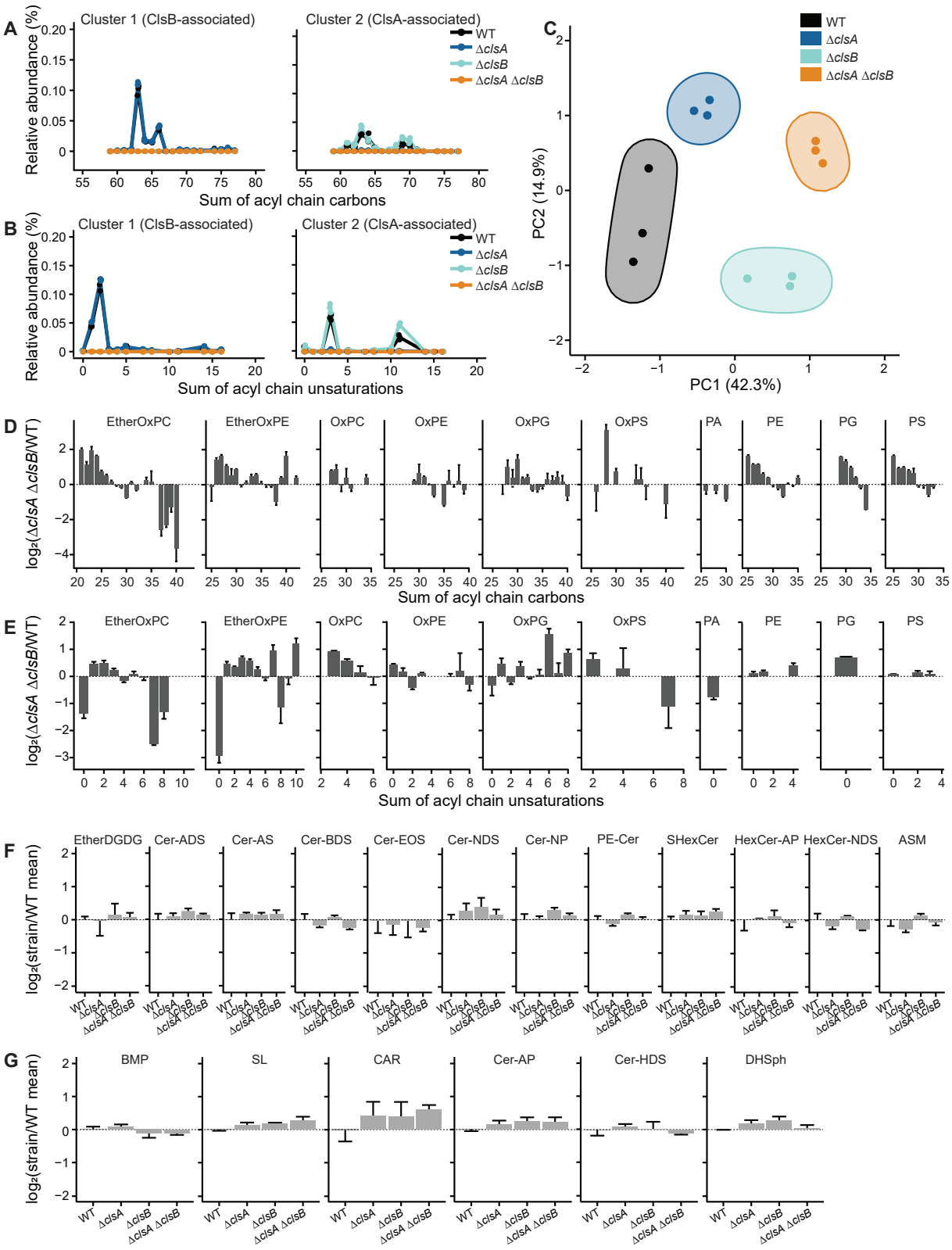
A
Cluster 1 (ClsB-associated)
Cluster 2 (ClsA-associated)
Relative abundance (%)
Sum of acyl chain carbons
WT
ΔclsA
ΔclsB
ΔclsA ΔclsB
B
Sum of acyl chain unsaturations
C
PC1 (42.3%)
PC2 (14.9%)
D
EtherOxPC
EtherOxPE
OxPC
OxPE
OxPG
OxPS
PA
PE
PG
PS
log2(ΔclsA ΔclsB/WT)
E
F
EtherDGDG
Cer-ADS
Cer-AS
Cer-BDS
Cer-EOS
Cer-NDS
Cer-NP
PE-Cer
SHexCer
HexCer-AP
HexCer-NDS
ASM
log2(strain/WT mean)
G
BMP
SL
CAR
Cer-AP
Cer-HDS
DHSph

1359 **Figure S7. Cardiolipin synthases produce unique lipid products and their loss remodels overall**
1360 **membrane lipid composition. A., B.** Relative abundance of lipids from K-means clusters 1 and 2 across
1361 *B. fragilis* WT, Δ*clsA*, Δ*clsB* and Δ*clsA* Δ*clsB* strains plotted by (**A.**) acyl chain length or (**B.**) acyl chain
1362 unsaturations. **C.** Principal component analysis plot of lipids in the *B. fragilis* membrane excluding
1363 cardiolipin and monolysocardiolipin species. Minimum volume-enclosing ellipses were estimated using
1364 the Khachiyan algorithm. **D., E.** $\log_2$(fold change) of Pa, PE, PG and PS lipids in Δ*clsA* Δ*clsB* cells
1365 compared to WT plotted by the sum of acyl chain (**D.**) carbons or (**E.**) unsaturations. **F., G.** $\log_2$(fold
1366 change) of lipids detected in (**F.**) negative or (**G.**) positive ionization modes with values for each strain
1367 compared to the mean abundance in WT cells. See figures 7 and S6 for lipid family abbreviations. Error
1368 bars indicate standard deviation. Unadjusted p-values are shown.

1369

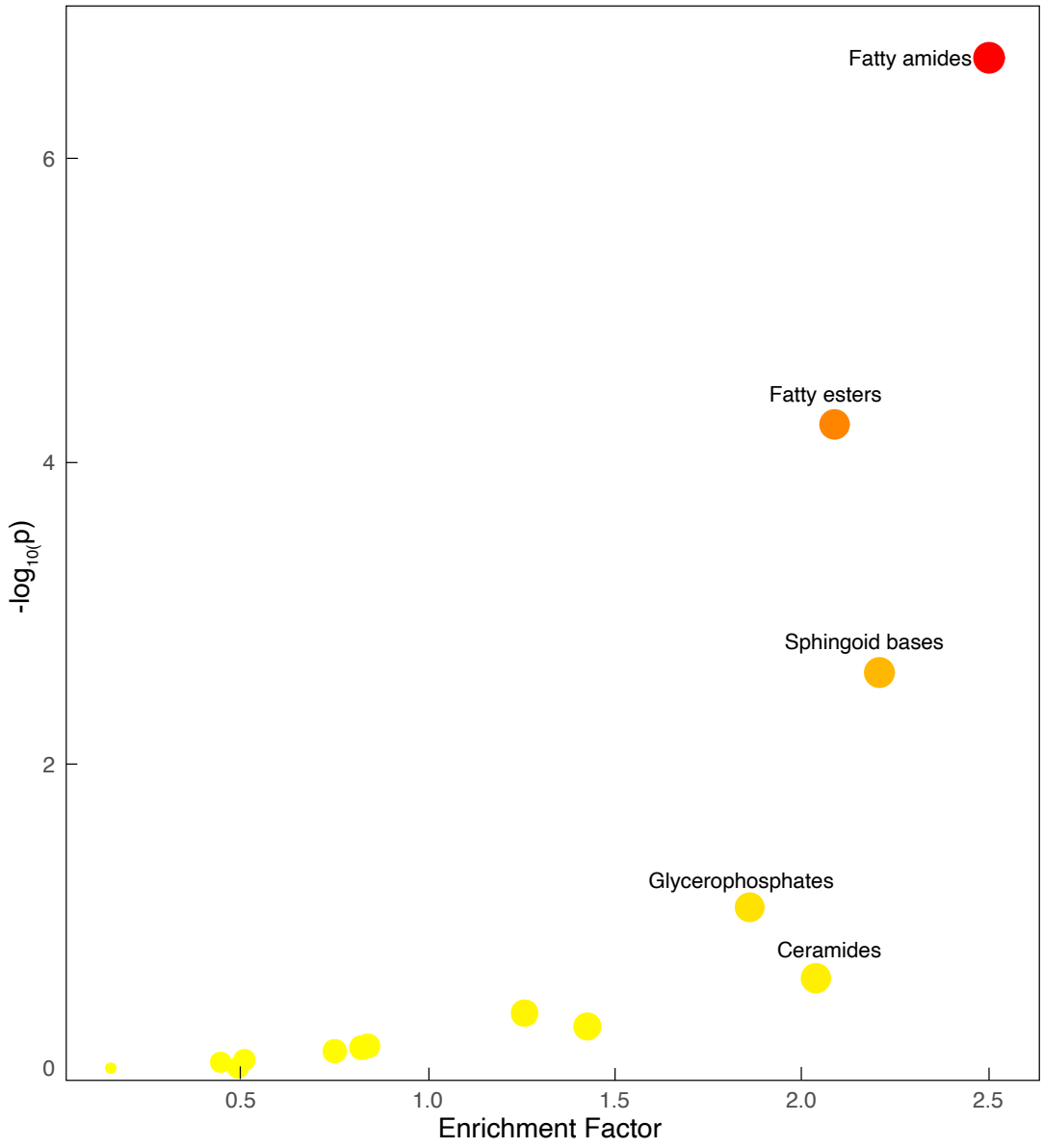

Figure S8. Pathway enrichment analysis for main lipid categories. Pathway analysis is performed with MetaboAnalyst 6.0, with default mummichog parameters with p-value cutoff of 0.0005 and lipid – main chemical class as the selected metabolite sets containing at least 3 entries.

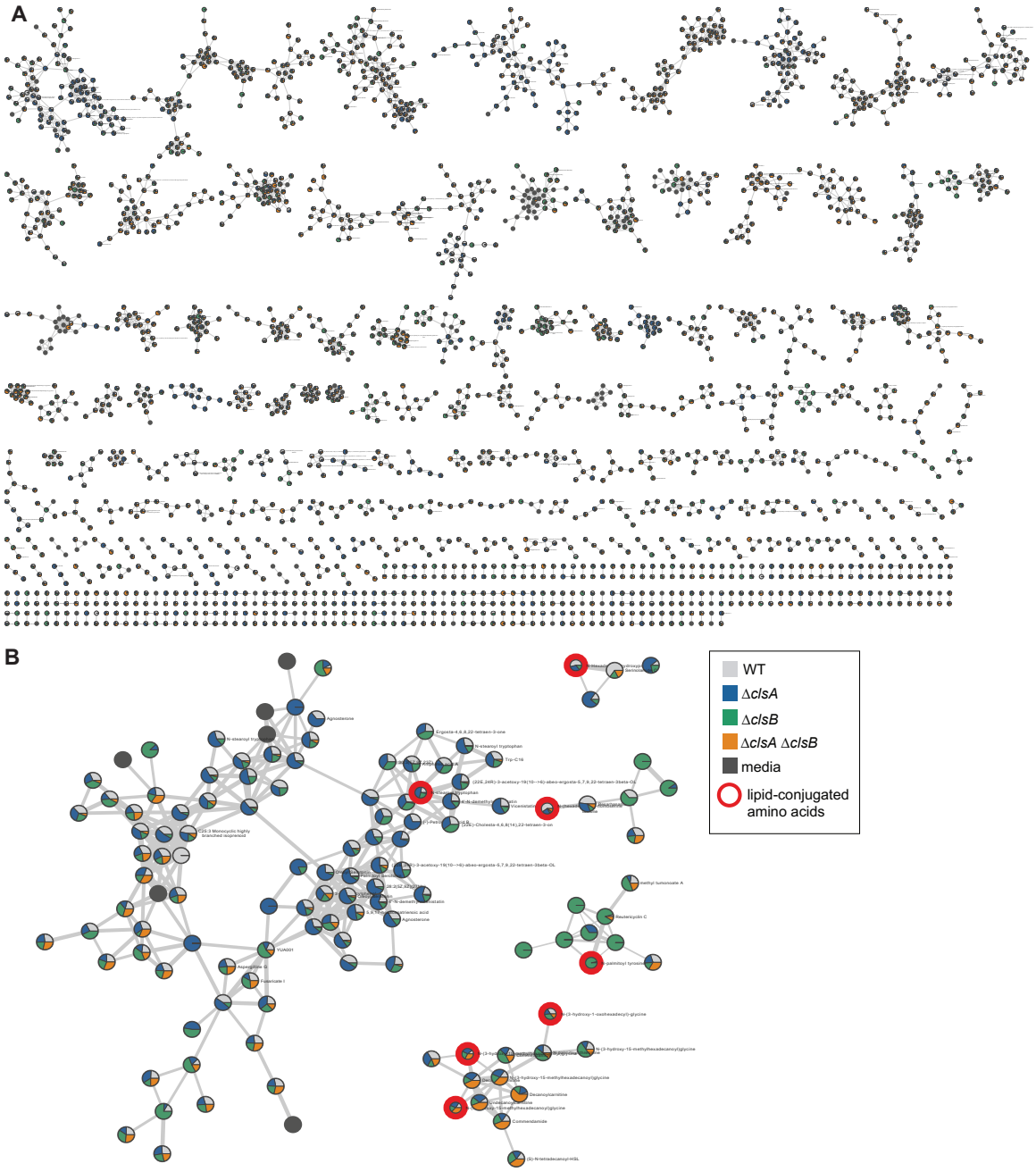

Figure S9. Molecular networking shows chemically related metabolites in *B. fragilis* strains. A. Feature-based molecular networking of all features (excluding singletons) from WT, Δ*clsA*, Δ*clsB*, Δ*clsA* Δ*clsB*, and extracted BHIS media. Each feature is a node, connected by an edge calculated from cosine

similarity score. **B.** Subset of features connected by an edge to fatty amides highlighted in Fig. 8 (red border). Each pie chart in the node is colored by relative abundance of the feature in each strain.

Table S1. Primers and vectors used in this study.

Table S2. Strains used in this study.

Table S3. Metadata for genomics analyses.

Table S4. Raw data for the lipidomics analyses.

Table S5. Raw data for the ICP-MS analyses.

Table S6. Raw data for untargeted metabolomics analyses.

Table S7. Pathway enrichment analysis for main lipid categories.

Table S8. Pathway enrichment analysis for sub non-lipid categories.